Synthetic Signatures of Volcanic Ash Cloud Particles From X-Band Dual-Polarization Radar

Frank Silvio Marzano, *Senior Member, IEEE*, Errico Picciotti, Gianfranco Vulpiani, *Member, IEEE*, and Mario Montopoli

***Abstract*—Weather radar retrieval, in terms of detection, estimation, and sensitivity, of volcanic ash plumes is dependent not only on the radar system specifications but also on the range and ash cloud distribution. The minimum detectable signal can be increased, for a given radar and ash plume scenario, by decreasing the observation range and increasing the operational frequency and also by exploiting possible polarimetric capabilities. For short-range observations in proximity of the volcano vent, a compact portable system with relatively low power transmitter may be evaluated as a suitable compromise between observational and technological requirements. This paper, starting from the results of a previous study and from the aforementioned issues, is aimed at quantitatively assessing the optimal choices for a portable X-band system with a dual-polarization capability for real-time ash cloud remote sensing. The physical–electromagnetic model of ash particle distributions is systematically reviewed and extended to include nonspherical particle shapes, vesicular composition, silicate content, and orientation phenomena. The radar backscattering response at X-band is simulated and analyzed in terms of self-consistent polarimetric signatures for ash classification purposes and correlation with ash concentration for quantitative retrieval aims. An X-band radar system sensitivity analysis to ash concentration, as a function of radar specifications, range, and ash category, is carried out in trying to assess the expected system performances and limitations.**

***Index Terms*—Ash clouds, backscattering modeling, meteorological radar, microwave systems, volcanic eruption.**

I. Introduction

THE RETRIEVAL of volcanic ash cloud properties is of significant interest due to their environmental, climatic, and socioeconomic effects [1]–[3]. Ash fallout can cause substantial hardship and damages in a volcano's surrounding area and can represent a serious hazard to aircraft as well [4]. Volcanic ash is usually composed of silicates (above all, aluminum and magnesium), and once they are sucked up by jet engines of modern airplanes, they can fuse in the combustion chamber in which temperatures may be as high as 1400 °C.

In order to monitor ash cloud pattern and concentration, satellite visible-infrared radiometric observations from geostationary satellites (e.g., Meteosat sensor) are usually exploited for long-range trajectory tracking and for measuring low-level eruptions [7]–[9]. Their imagery is available every 15–30 min and suffers from a relatively poor spatial resolution (i.e., on the order of some kilometers). Moreover, the field-of-view of geostationary radiometric measurements may be blocked by water and ice clouds at higher levels, and their overall utility is reduced at night. Satellite data from radiometric sensors aboard near-polar orbiting platforms can also be employed to detect and map volcanic ash clouds over the entire globe [9]–[11]. The usefulness of these sensors is limited by their relatively poor temporal resolution, guaranteeing only two overpasses per day at most using a single platform.

Many volcanic cloud encounters have happened only minutes to a few hours after eruptive events so that timely information on the eruption's onset and its intensity is vital [12]. Among the remote sensors, ground-based microwave weather radars may represent an important tool to detect and, to a certain extent, mitigate hazards from the ash clouds [13]–[19], [52]. The possibility of monitoring in all weather conditions at a fairly high spatial resolution (less than a few hundreds of meters) and every few minutes after the eruption is the major advantage of using ground-based microwave radar systems. Ground-based weather radar systems can also provide data for determining the ash volume, total mass, and height of eruption clouds. The latter information is particularly valuable because a series of column height measurements allows the mass and dynamics of an eruption to be directly monitored. Moreover, the altitude of the cloud top above the vent represents an essential datum both to aviation safety and early warning and to ash cloud trajectory models that are able to forecast the position of volcanic clouds after an eruption based on winds aloft. In this respect, other ground-based microwave instrumentation, such as the ground-based lidar optical systems, may show a higher sensitivity to ash contents with respect to microwave instruments [20], [21]. However, the lidar higher sensitivity is counterbalanced by stronger path attenuation effects when the ash cloud is composed of coarse ash (CA) and small lapilli (SL), particularly in proximity of the volcano vent, and when water clouds are also present. The weather radar and lidar systems are, in a way, complementary due to their

Manuscript received September 11, 2010; revised March 24, 2011; accepted May 29, 2011. Date of publication August 8, 2011; date of current version December 23, 2011. This work was supported in part by the Italian Department of Civil Protection (Rome, Italy) within the IDRA project and in part by Sapienza University of Rome (Rome, Italy).

F. S. Marzano is with the Department of Information Engineering, Electronics and Telecommunications, Sapienza University of Rome, 00184 Rome, Italy, and also with CETEMPS, University of L'Aquila, 67040 L'Aquila, Italy (e-mail: marzano@diet.uniroma1.it).

E. Picciotti is with HIMET, 67100 L'Aquila, Italy, and also with CETEMPS, University of L'Aquila, 67040 L'Aquila, Italy (e-mail: errico.picciotti@himet.it).

G. Vulpiani is with the National Department of Civil Protection, 00189 Rome, Italy (e-mail: gianfranco.vulpiani@protezionecivile.it).

M. Montopoli is with the Department of Electrical and Information Engineering and CETEMPS, University of L'Aquila, 67040 L'Aquila, Italy (e-mail: mario.montopoli@univaq.it).

Color versions of one or more of the figures in this paper are available online at http://ieeexplore.ieee.org.

Digital Object Identifier 10.1109/TGRS.2011.2159225

different sensitivity to coarse-to-large and to FA-to-CA particles, respectively.

The use of weather radars to observe ash eruptions is quite limited indeed, and most radar observations of volcanic eruptions are occasionally carried out by meteorological radars of national weather services. During the Mount St. Helens volcanic activity in 1980–1982, there was a unique opportunity to collect observations using the U.S. National Weather Service radar system at C-band in Portland, OR [13]. Recently, the explosive eruptions of the Icelandic Hekla volcano in 2000 [14], the Grimsovtn volcano in 2004 [22], and the Augustine volcano in Alaska in 2008 [22] were investigated through weather radar measurements. In spite of this potential and the fact that weather radar use dates back to the early 1980s, there are still open issues about microwave weather radar capabilities to quantitatively retrieve volcanic ash cloud parameters.

The purpose of previous methodological studies was the possibility of using a ground-based single-polarization radar system for the remote sensing of volcanic ash cloud [15], [24]. A microphysical characterization of volcanic ash was carried out in terms of dielectric properties, size distribution (i.e., Gamma or Weibull functions), and terminal fall speed, assuming spherically shaped particles [24]. Specific applications were also evaluated to assess the radar sensitivity as a function of volcanic ash mass range profiles by using the technical characteristics of three weather radars at S-, C-, and X-bands. A prototype of the volcanic ash radar retrieval (VARR) algorithm was finally structured and argued, under the already mentioned assumptions [15]. The VARR approach and its extensions can be a useful tool to interpret reflectivity measurements in term of concentrations and ashfall rate within a general volcanic ash monitoring strategy.

Radar volcanology can exploit recent developments of radar meteorology in terms of radar response modeling and system advancements. In particular, polarimetry has received a lot of attention in radar meteorology (e.g., [25] and [26]). The dual-polarization capability can be exploited to measure not only horizontally polarized reflectivity but also differential reflectivity, differential phase shift, copolar correlation coefficient, and linear depolarization ratio (LDR) (e.g., [27]–[29]). The success of radar polarimetry for rainfall observation is due to the prevailing oblateness of raindrops. At the equilibrium, a relation between the axial ratio of a spheroid and the diameter of an equivolume sphere can be theoretically derived and experimental oscillations around this shape may introduce some random variations [28]. Tumbling effects are typical of less dense hydrometeors such as graupel and hail. In this respect, volcanic ash particles exhibit shapes and orientations which are dictated by their explosive origin [12]. Their aspect ratio (AR) may be significantly nonspherical, but at the same time, depending on the type of eruption and pyroclasts [30]–[35]. Finer ash particles may be characteristic of a laminar fallout, while bigger particles can be typical of near-vent plume dominated by convective activity [32]. These conditions may affect the particle orientation and aggregation processes [35].

Weather radar sensitivity to ash minimum concentration is basically dependent on the minimum detectable signal (MDS) [37]. The latter can be increased, for a given radar and ash plume scenario, by decreasing the range and increasing the frequency. In case of ash plume radar monitoring, frequencies higher than the X-band may suffer the problem of two-way path attenuation effects which may strongly degrade the retrieval product accuracy [24]. The range choice is a problematic tradeoff, as for a fixed radar system, since the volcano itself may cause a beam obstruction and the plume may advect in unknown directions. A way to approach this problem is to resort to X-band portable systems which has recently gained a renewed interest in radar meteorology (e.g., [38]–[40]). In this respect, the choice of frequencies higher than C-band may help to reduce the overall sizes of the radar system. For short-range observations, a relatively low power transmitter can also be chosen with a peak power equal or less than 50 kW (instead of 250 kW, typical of C-band systems) [38]. From what was exposed earlier, it seems that the choice of a portable X-band weather Doppler polarimetric radar system may satisfy both technological and new scientific requirements.

This work starts from the results of the previous study and from aforementioned issues and is aimed at the following: 1) summarizing in a systematic way the physical properties and polarimetric electromagnetic models of ash particle polydispersions; 2) analyzing the model-based dual-polarization radar signature of ash particle volumes in terms of statistical properties, discrimination capability, and correlation features; and 3) quantitatively assessing the optimal choices for a portable X-band system with a dual-polarization capability for real-time ash cloud remote sensing.

This paper is organized as follows. In Section II, the physical model of ash particles is extended to include nonspherical shapes and orientation phenomenology with the aim to provide a systematic characterization of ash particle properties in a way similar to what was done for hydrometeors by Straka *et al.* [27]. In Section III, the backscattering response at X-band is simulated and analyzed in terms of polarimetric signature and correlation with ash concentration. In Section IV, an X-band radar system sensitivity is carried out, whereas Section V is dedicated to summary and conclusion.

II. Ash Particle Modeling

A volcanic eruption is a geological phenomenon that consists of the liberation of magma from the deep layers of the Earth through openings or fissures of the terrestrial crust [12]. In explosive form, an eruption throws up lava or pieces of rock, called pyroclastics which may be incandescent.

Volcanic ash clouds are formed during explosive volcanic eruptions [35]. Explosive eruptions occur when gases dissolved in molten rock (magma) expand and escape violently into the air and also when water is heated by the magma and abruptly flashes into steam. Once in air, hot ash and gas rise quickly to form a towering eruption column, commonly several kilometers high. However, wind can quickly blow fine ash (FA) away from the volcano to form an eruption cloud. As the cloud drifts downwind from the erupting volcano, the ash that falls from the cloud typically becomes smaller in size and forms a thinner suspended layer [41].

TABLE I
MAIN CHARACTERISTICS OF VOLCANIC PYROCLASTS (ADAPTED FROM [12])

TEPRHA	Particle type	Particle size	Distance from the volcano vent	Residence time in the atmosphere
Ash	*Fine ash (FA)*	Less than 64 μm	Hundred to thousand kilometers	Day to month
	Coarse ash (CA)	From 64 μm to 532μm	Ten to hundred kilometers	Day
Lapilli	*Small lapilli (SL)*	From 0.532 mm to 2.56 mm	Few to ten kilometers	Few minutes
	Large lapilli (LL)	From 2.56 mm to 32 mm	Hundred meters to few kilometers	Seconds to minutes
Blocks	*Blocks and bombs (BB)*	Greater than 32 mm	Ten to hundred meters	Tens of seconds

A. Physical Properties

Materials of all types and sizes, erupting from a crater or volcanic vent as a result of an intensive magma and rock fragmentation, are usually referred to as tephra [42]. This term describes volcanic ash and coarser detritus that are projected through the air. Tephra is chiefly characterized by clast size, shape, vesicularity, and composition [43]–[45].

The diameters of particles in fall deposits typically range from a few micrometers or less to several centimeters or more [30]–[34]. Both the concentration and diameter of particles in the volcanic clouds decrease with distance from the vent because larger particles tend to fall out quickly. Table I summarizes typical diameters, residence period in atmosphere, as well as the distance from the vent that volcanic debris can reach [12]. Ash are generally very fine-grained fragments (< 2 mm) and are generally dominated by broken glass shards, but with variable amounts of broken crystal and lithic (rock) fragments. Lapilli may look like cinders, and within water-rich eruptions, the accretion of wet ash may form rounded spheres known as accretionary lapilli. Larger erupted materials, like bombs, have shapes or textures such as vesicularity that indicate they were liquid or plastic when erupted. Blocks, generally, are more angular and solid when erupted.

Volcanic clouds may contain a variety of components including the following: 1) volcanogenic products from the eruption: volcanic gases, pyroclasts, and aerosol particles derived from reactions of volcanogenic and atmospheric materials and 2) products from the ambient atmosphere, such as water (vapor, liquid, and ice) and gaseous species and various particles from the land and sea including wind-blown silicates, sea salt, and others [12]. Volcanogenic silicate particles in volcanic clouds consist of fine pyroclasts, salts, and acids in aerosol form. Direct sampling of volcanogenic particles has only rarely been accomplished by balloon studies and a few research aircraft. *In situ* airborne ash has also been recovered from the air filters of a few aircraft that have penetrated volcanic ash plumes (e.g., [46]).

The particles consist of two main types: silicate and nonsilicate particles. Silicate particles represent fragments of the magma [35]. These are glassy pyroclasts and minerals, which represent the crystalline fraction of the magma with angular shape. Generally speaking, basaltic and andesitic eruptions tend to give rise to particles with moderate ARs, whereas rhyolitic eruptions can generate an abundance of glassy pyroclasts with a platy geometry and extreme ARs [47]. The diameters of silicate pyroclasts generated during explosive eruptions range from micrometers to meters. Those in volcanic clouds are smaller, generally less than about 50 μm. The mass proportions of silicate particles with diameters less than about 1 μm are very small. Nonsilicate particles are related to reactions among the constituents of the volcanic gases. These particles are generally smaller than the silicates, usually less than 1 μm in diameter. The most common composition for these is sulfate, particularly H_2SO_4, which forms as submicrometer spherical droplets which also contain H_2O (typically about 25% by volume) [48]. Aside from these two broad types, a wide variety of other unexplained materials have been observed in volcanic clouds. They consist largely of phases that are amorphous and have uncertain compositions [32]. Many or most of these particles are likely to be nonvolcanic in origin and represent accidental material of superficial or extraterrestrial origin.

Volcanic ash is formed by volcanoes through several different processes that transform large batches of magma and country rock into smaller pieces [42]. The two general mechanisms can be identified as follows.

1) Magmatic fragmentation, in which the evolution and expansion of magmatic gases contribute to volcanic ash production. Ash particles are usually marked by the presence of vesicles and production of pumice.
2) Phreatomagmatic fragmentation, in which physical contact and mixing of magma with external water results in ash particle formation. The propagation of stress waves through the magma and instabilities at the interfaces between magma and water can contribute to ash production.

Volcanic ash particles have a wide distribution of shapes and sizes. Since the airborne ash particles are difficult to collect, the only samples available for direct measurements are usually taken from the ground. One of the major sources of quantitative information on ash particles is the work of Riley *et al.* [34]. They studied three main sources as schematically summarized next.

1) *Volcan Fuego, Guatemala*. The basaltic October 14, 1974 Fuego ash was produced by a sulfur-rich sub-Plinian eruption that reached a height of 18 km above sea level. Basalt is a hard black volcanic rock, where less than 50% of its weight is silica (due to low silica content, basalt has a low viscosity). The eruption injected a 0.03-km^3 dense

rock equivalent (DRE) of ash into the atmosphere over a period of 5 h.

2) *Mount Spurr, Alaska*. The August 18, 1992 Spurr eruption has the most robust data set of the three eruptions in this study. Over 50 fallout andesite samples were collected within 48 h following the eruption from 2 to 300 km from the volcano. Andesite has a silica content of 57% (it is in the intermediate category of the silicic–mafic scale). The sub-Plinian eruption from the Crater Peak vent at Mount Spurr erupted 14×10^6 m^3 DRE of pyroclastic material. The plume reached the stratosphere at a peak altitude of at least 13.7 km above sea level.
3) *Ash Hollow Member, Nebraska*. The late Miocene (9–11 Ma) Ogallala Formation contains at least ten ash members which extend from Nebraska to Texas, covering thousands of square kilometers. The Ash Hollow Member is the topmost ash unit of the Ogallala Formation and is of rhyolitic composition. Rhyolite has a silica content greater than about 68% (rhyolite eruptions often produce pumice or obsidian).

Another notable source of information was the 2001/2002 Mount Etna eruption fall deposits in Italy studied by several authors [49], [50]. Note that, besides basalt, andesite, and rhyolite, there are other intermediary igneous volcanic rocks, such as dacite (with about 63%–68% of silica content, predominant in the Pinatubo eruption on 1991 [12]) which will not be considered in this work due to a lack of available data on dacite particle distributions.

B. Shape and Orientation

The AR tells us about the shape and surface area of a particle [34]. The wide variability in ARs measured for nonvesicular particles of the Ash Hollow sample and low terminal velocity particles in the Spurr and Fuego samples suggest that these particles have shapes whose form is greatly influenced by relict bubble walls (fragmentation by expanding gases in the magma would cause breakage along irregularly distributed vesicles and concave-shaped bubble walls).

We can try to model the correlation of AR with other size parameters for particle diameters less than 0.2 mm. For remote sensing applications, the use of the AR data has improved calculations for effective radius and volcanic cloud mass concentrations [36]. If we collect all the measured AR and diameter data from Riley *et al.* [34], we can derive a simple regression formula which relates the axis ratio $r_{\mathrm{ax}} = l/w$ (length l over width w) to the spherical volume-equivalent diameter D_e

$$r_{\mathrm{ax}-b} = \frac{l}{w} = \begin{cases} 1.64, & \text{for } D_e < 0.01 \text{ mm} \\ 1.66 - 1.55 D_e, & \text{for } 0.01 < D_e < 0.2 \text{ mm} \\ 1.40, & \text{for } D_e \geq 0.2 \text{ mm} \end{cases}$$

$$r_{\mathrm{ax}-r} = \frac{l}{w} = \begin{cases} 1.56, & \text{for } D_e < 0.01 \text{ mm} \\ 1.45 + 11.03 D_e, & \text{for } 0.01 < D_e < 0.2 \text{ mm} \\ 2.40, & \text{for } D_e \geq 0.1 \text{ mm} \end{cases} \quad (1)$$

where $r_{\mathrm{ax}-b}$ and $r_{\mathrm{ax}-r}$ stand for axial ratio of basaltic–andesitic and rhyolitic particles, respectively. The rationale of this formula is shown in Fig. 1, and it suffers the limitation due to the lack of data for particles larger than 0.2 mm so that we have arbitrarily extrapolated constant values outside the measured size interval. Considering the Fuego/Spurr and Hollow data, the root mean square errors for the estimate of axial ratio in (1) are 0.0446 and 0.1021 (adimensional), respectively. The AR has been also investigated by Krotkov *et al.* [36], confirming the range of variability shown in (1).

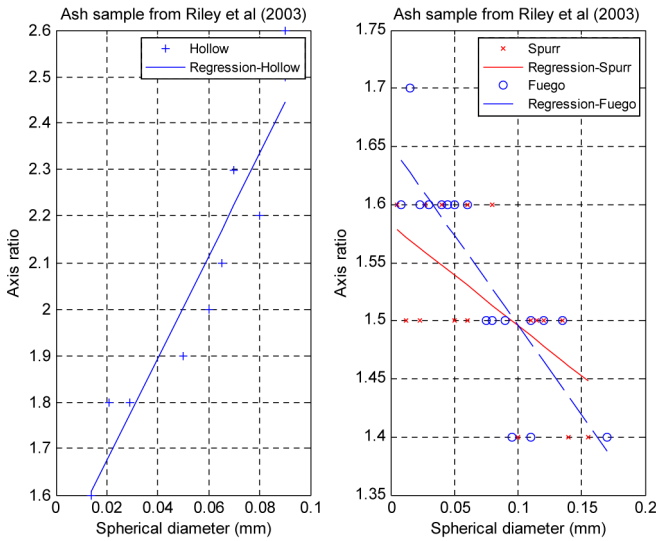

Fig. 1. Axis ratio versus spherical volume-equivalent diameter of ash particles, derived from experimental measurements of Riley *et al.* [34] on Volcan Fuego, Mount Spurr, and Ash Hollow ash fallout and their regression curves (see text for details).

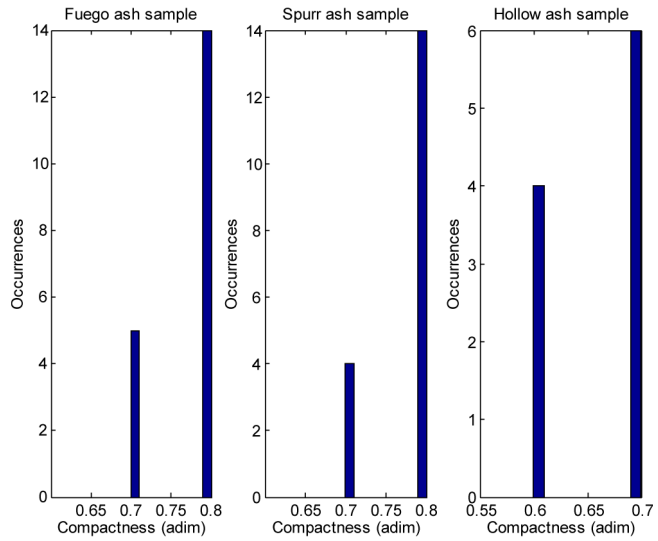

Fig. 2. Histogram of ash particle compactness measurements, derived from experimental measurements of Riley *et al.* [34] taken at the Volcan Fuego, Mount Spurr, and Ash Hollow sites (see text for details).

A further parameter of interest to describe the particle appearance in terms of its vesicularity is the compactness ratio r_{comp}, defined as the ratio between the 4π times area and the square convex perimeter [34]. In case of homogeneous compact spherical particles, $r_{\mathrm{comp}} = 1$. From the samples analyzed in [34], we can plot the histogram of r_{comp}, as reported in Fig. 2.

The mean of $r_{\rm comp}$ ranges from 0.66 to 0.76 with a maximum variation between 0.6 and 0.8.

Information on the ash particle orientation distribution (POD) during the ashfall is practically nonexistent [12]. In a conservative way, we may assume that a solid particle may undergo the following:

1) *uniform tumbling orientation* during high convection so that it is randomly oriented without a preferential axis;
2) *oblate orientation* where the symmetry axis of the particle (if any) is parallel to the Earth surface or orthogonal to the gravitational forces with some oscillations within the main asset;
3) *prolate orientation* where the symmetry axis of the particle (if any) is orthogonal to the Earth surface or parallel to the gravitational forces with some oscillations within the main asset.

An analytical model of POD may be described by the probability density function (PDF) $p_p(\phi)$ of the particle canting angle ϕ between the vertical (altitude) axis and the particle symmetry axis [26].

A common choice is to assume this probability density equal to a normalized Gaussian function with m_ϕ and σ_ϕ being the mean and the standard deviation of ϕ. Alternative to this, we may use a uniform PDF with Δ_ϕ as the interval of uniform variation of ϕ. Note that $p_p(\phi)$ is normalized to 1 over the solid angle and that, when integrating in the spherical angular coordinate (θ_b, φ_b) of the body under the assumption of independent azimuth and zenith PDFs, this normalization is equal to 1 [26]. This implies that the canting angle ϕ can be assumed equal to the zenith angle θ_b. Using the previous PDF model of canting angles, we may define the following:

1) *tumbling orientation* (TO) where the Gaussian PDF (G-PDF) has $m_\phi = 45^\circ$ and large σ_ϕ (about 30°);
2) *oblate orientation* (OO) where the G-PDF has $m_\phi = 0^\circ$ and relatively small σ_ϕ (about 10°);
3) *prolate orientation* (PO) where the G-PDF has $m_\phi = 90^\circ$ and relatively small σ_ϕ (about 10°).

C. Composition and Size Distribution

There is a fairly large consensus about the capability to model the particle size distribution (PSD) through either a normalized Gamma or Weibull size distribution (e.g., [24],[35], and [42]). In case of a multimode size distribution, it is always possible to suppose more than one analytical PSD characterized by different mean sizes and total number of particles.

In this paper, we have adopted the scaled-Gamma (SG) PSD as a general model both for ash and hydrometeor particles. If D_e is the diameter of a spherical volume-equivalent particle, the SG-PSD N_p for a generic class of ash particles p can be written as [24]

$$N_p(D_e) = N_{np}\left(\frac{D_e}{D_{\rm np}}\right)^{\mu_p} e^{-\Lambda_{\rm np}\left(\frac{D_e}{D_{\rm np}}\right)} \tag{2}$$

where the "intercept" parameter $N_{\rm np}$ and the "slope" parameter $\Lambda_{\rm np}$ in a logarithmic plane are related to the "shape" parameter μ_p and to the particle density ρ_p through

$$\begin{cases} N_{\rm np} = 10^6 \frac{6C_p\Lambda_{\rm np}^{\mu_p+4}}{\pi\rho_p D_{\rm np}^4\Gamma(\mu_p+4)} \\ \Lambda_{\rm np} = \mu_p + 1 \end{cases} \tag{3}$$

with C_p as the mass concentration and $D_{\rm np}$ as the number-weighted mean diameter. It is worth mentioning that $N_{\rm np}$ has a dimension which is μ_p independent and usually given in $\rm mm^{-1}m^{-3}$, Λ_{np} is adimensional, and $N_p(D)$ is completely specified by the three parameters μ_p, $D_{\rm np}$, and C_p (assuming a constant density ρ_p).

Let us assume that the following are true: 1) Particles are spherical or equivalent spherical so that their mass is $m_p = \rho_p(\pi/6)D^3$ with a constant density ρ_p, and 2) the minimum and maximum diameters are zero and infinite so that the complete moment $m_{\rm np}$ of order n of N_p can be expressed by [15], [22]

$$m_{\rm np} = \frac{N_{\rm np}D_{\rm np}^{n+1}}{\Lambda_{\rm np}^{n+\mu_p+1}}\Gamma(n+\mu_p+1) \tag{4}$$

where $\Gamma(n+1) = n!$ if n is an integer. Using (4), the total volumetric number of particles $N_{\rm tp}$ (in per cubic meter) is $N_{\rm tp} = m_{0p}$, whereas the *mass concentration* C_p (in grams per cubic meter) is given by $C_p = \pi/6\rho_p m_{3p}$ and the number-weighted mean diameter $D_{\rm np}$ (in millimeters) is defined by $D_{\rm np} = m_{1p}/m_{0p}$. The particle fall rate R_p $[\rm kg\cdot h^{-1}\cdot m^{-2}]$, defined as the particle mass crossing a horizontal cross section of unit area over a given interval of time, can be expressed through the moment m_{3+bv}, where $v_p(D_e) = a_v D_e^{b_v}$ $[\rm m\cdot s^{-1}]$ is the terminal fall velocity in still air of ash particles. The best fitting of *in situ* data of ashfall terminal velocity as a function of ash diameter provides $a_v = 5.558$ $\rm m\cdot s^{-1}$ and $b_v = 0.722$ from the year 1982 data of the Mount St. Helens eruption [13], [15].

D. Dielectric Constant

The knowledge of the dielectric properties of volcanic ashes is of extreme importance for remote sensing of eruption columns and ash clouds in the atmosphere with meteorological radar systems [13]. In particular, this application requires a dielectric constant of a solid rock equivalent of a dilute volcanic ash suspended in air in order to compute the radar reflectivity. Adams *et al.* [51] extended previous data to include a wavelength range of 1.5–7.5 cm (frequency range of 4–19 GHz) and volcanic ash compositions of 0%–75% silica. To obtain an effective dielectric constant, they used a microwave technique placing a quantity of volcanic ash in a shorted waveguide. The standing wave which results will have its nulls shifted, which is a consequence of the real part of the complex dielectric constant of the ash. The ratio of the maximum electric field to the minimum (the standing wave ratio) will decrease as a result of the presence of losses in the ash, which is a consequence of the imaginary part of the complex dielectric constant. In order to determine the actual relative permittivity $\varepsilon_{\rm ras}$ of the ash solid volcanic particle, a mixing formula was used to relate the

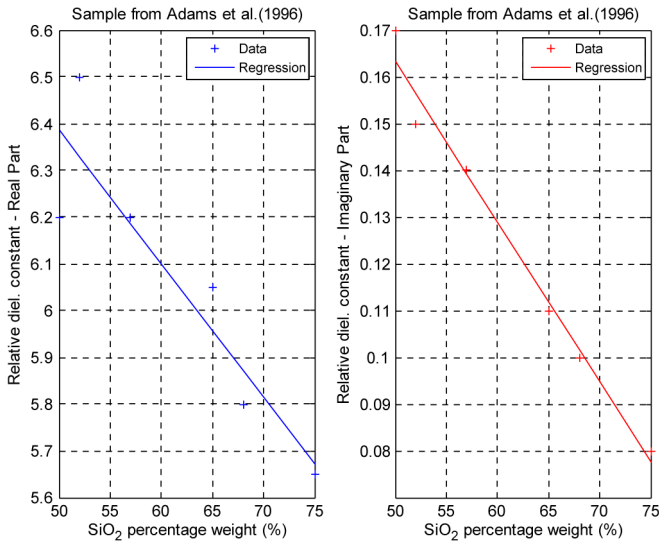

Fig. 3. Real and imaginary parts of the complex permittivity of volcanic ash, as a function of percent SiO_2, using data reported by Adams *et al.* [51], and their regression curves (see text for details).

measured permittivity and porosity of the ash and air mixture to a specific solid-ash value.

These measurements of the real and imaginary parts of the complex dielectric constant of powdered volcanic ash samples indicate that, to within experimental uncertainty, these parameters are essentially independent of frequency in the C-, X-, and Ku-bands. Using data from [51], the linear relationship between the chemical composition of volcanic ash and the ash permittivity has been identified, as shown in Fig. 3, for the ash samples considered herein. Within the range 50%–75% of SiO_2, the real and imaginary parts are, respectively, about 15% and twice higher for ash with lower silica content. From the previous figure, we can extract a SiO_2 weight dependence for the real $\varepsilon'_{\rm ras}$ and the imaginary $\varepsilon''_{\rm ras}$ part

$$\begin{cases} \varepsilon'_{\rm ras} = a_0 + a_1 W_{\rm Si02} \\ \varepsilon''_{\rm ras} = b_0 + b_1 W_{\rm Si02} \end{cases} \tag{5}$$

where a_i and b_i are regression coefficients and $W_{\rm SiO2}$ (in percent) is the percentage weight of SiO_2. The coefficients in (5) are as follows: $a_0 = 7.81$ and $a_1 = -0.028$, and $b_0 = 0.335$ and $b_1 = -0.0034$.

Mixing formulas, such as that of Maxwell–Garnett, might be used for modeling the relative dielectric constant of a mixture of ash with some inclusions. At the first order and for spherical inclusions, if the mass fraction of inclusions is f_i, the Maxwell–Garnett formula for a particle mixture dielectric constant $\varepsilon_{\rm rp}$ is expressed by

$$\varepsilon_{\rm rp} = \varepsilon_{\rm ras}(1 - f_i) + f_i \varepsilon_{\rm ri} \tag{6}$$

where $\varepsilon_{\rm ras}$ is the dielectric constant of solid ash and $\varepsilon_{\rm ri}$ is the dielectric constant of the inclusions. The latter may be air, glass, and minerals. In case of air, the relative dielectric constant $\varepsilon_{\rm ri} \cong 1.00054$. The previous Maxwell–Garnett formula is mainly valid at low frequencies, but for our purposes, it is a reasonable first-order approximation. The inclusion fraction f_i may be heuristically represented through the compactness index of ash particles that may vary between 0.6 and 0.8 [34]. If we assume that

$$f_i = 1 - r_{\rm comp} \tag{7}$$

then f_i may vary between 0 and 0.3. If $f_i = 0$, the particle is made of pure solid ash, as obvious. A variability of inclusion fraction f_i between 0 and 0.3 may be expected and assumed as a first-order approximation.

For radar applications, it is important to estimate the ash complex dielectric factor K_p of ash particles, defined as

$$|K_p|^2 = \left|\frac{\varepsilon_{\rm rp} - 1}{\varepsilon_{\rm rp} + 2}\right|^2 = \left|\frac{(\varepsilon'_{\rm rp} - j\varepsilon''_{\rm rp}) - 1}{(\varepsilon'_{\rm rp} - j\varepsilon''_{\rm rp}) + 2}\right|^2 \tag{8}$$

where $\varepsilon'_{\rm rp}$ and $\varepsilon''_{\rm rp}$ are the real and the imaginary part of the ash relative dielectric constant $\varepsilon_{\rm rp}$. From S- to K-band, the real part $\varepsilon'_{\rm ras}$ ranges from 5.5 to 6.5, while the complex part $\varepsilon''_{\rm ras}$ ranges from 0.08 to 0.17 [51]. Thus, the solid-ash dielectric factor K_{as} of solid ash can range from about 0.37 to 0.41, basically depending on silicate contents through (5). This implies that, on average, it holds $|K_{\rm as}|^2 = 0.39 \pm 0.02$, regardless of composition or wavelength.

In order to model vesicular microphysical effects, we can assume ash particles as a mixture of solid ash and air with ρ_p as the mixture particle density and $\rho_{\rm as}$ as the solid-ash density. The ratio K_p/ρ_p of the ash mixture may be assumed equal to the sum of the ratios corresponding to solid ash and air weighted by their relative mass [24]. Since $|K_{\rm air}|^2 \cong 0$, it yields

$$K_p \cong \frac{\rho_p}{\rho_{\rm as}}\left(\frac{m_{\rm as}}{m_p}\right) K_{\rm as} \cong \rho_p(1 - f_i)\left(\frac{\varepsilon_{\rm ras} - 1}{\varepsilon_{\rm ras} + 2}\right) \tag{9}$$

where $m_{\rm as}$ and m_p are the solid-ash and mixture particle masses, respectively, f_i is the air-inclusion fraction due to vesicular effects and, in the last term, the solid-ash density $\rho_{\rm as}$ has been put equal to 1 g/cm^{-3}. A further model improvement might be to let ρ_p be inversely dependent on particle diameter (bigger particles are generally less dense).

In this paper, we have avoided the treatment of aggregation between ash and water particles, which has been preliminarily considered elsewhere in terms of radar response effects [22]. Indeed, the analysis of hydrometeor aggregation processes is fairly cumbersome and with even less information available from both theoretical and experimental points of view [35].

E. Supervised Random Characterization

After summarizing the physical and dielectric properties of ash particles, we need to set up a statistical model of their main descriptive parameters. The aim is to realize a Monte Carlo random generation of ash particle ensembles and then use this physically oriented database to train the VARR algorithm. From Section II-A–D, the minimum significant number of ash parameters we can identify (to the state of current knowledge) is given in Table II and listed as follows: 1) PSD mean diameter $D_{\rm np}$; 2) mass concentration C_p; 3) PSD shape parameter μ_p; 4) particle density ρ_p; 5) POD mean canting

TABLE II

OVERVIEW OF SUPERVISED ASH CLASS PARAMETERIZATION WITH THE LIST OF THE MAIN VARIABLES AND THEIR ASSUMED STATISTICAL CHARACTERIZATION, EITHER DERIVED FROM LITERATURE [34], [42], [50], [51] OR HEURISTICALLY DETERMINED [15]. NOTE: PDF STANDS FOR PROBABILITY DENSITY FUNCTION, SG-PSD FOR SCALED-GAMMA PARTICLE SIZE DISTRIBUTION, m_x FOR MEAN OF x, σ_x FOR STANDARD DEVIATION OF x, AND AR FOR PARTICLE ASPECT AXIS RATIO

Property	*Fine ash (FA)*	*Coarse ash (CA)*	*Small lapilli (SL)*	*Large lapilli (LL)*
Ash diameter mean and deviation m_{Dn} (mm) and σ_{Dn} (mm)	*Gaussian PDF* m_{Dn}=0.01 σ_{Dn}=0.3m_{Dn}	*Gaussian PDF* m_{Dn}=0.1 σ_{Dn}=0.3m_{Dn}	*Gaussian PDF* m_{Dn}=1 σ_{Dn}=0.3m_{Dn}	*Gaussian PDF* m_{Dn}=10 σ_{Dn}=0.3m_{Dn}
Ash particle concentration mean and deviation m_{Cp} (mm) and σ_{Cp} (g/m^3) SC : Small Concentration MC: Medium Concentration IC : Intense Concentration	*Gaussian PDF* σ_{Cp}=0.3m_{Cp} *SC:* m_{Cp}=0.1 *MC:* m_{Cp}=1 *IC:* m_{Cp}=5	*Gaussian PDF* σ_{Cp}=0.3m_{Cp} *SC:* m_{Cp}=0.1 *MC:* m_{Cp}=1 *IC:* m_{Cp}=5	*Gaussian PDF* σ_{Cp}=0.3m_{Cp} *SC:* m_{Cp}=0.1 *MC:* m_{Cp}=1 *IC:* m_{Cp}=05	*Gaussian PDF* σ_{Cp}=0.3m_{Cp} *SC:* m_{Cp}=0.1 *MC:* m_{Cp}=1 *IC:* m_{Cp}=5
Ash size distribution shape parameter μ_p (adimensional)	*Scaled Gamma PSD* μ_p = *1-2, U-PDF*	*Scaled Gamma PSD* μ_p = *1-2, U-PDF*	*Scaled Gamma PSD* μ_p = *1-2, U-PDF*	*Scaled Gamma PSD* μ_p = *1-2, U-PDF*
Ash particle density ρ_p (g/cm^3)	*Uniform PDF* ρ_p= *0.5-2.5*	*Uniform PDF* ρ_p= *0.5-2.5*	*Uniform PDF* ρ_p= *0.5-2.5*	*Uniform PDF* ρ_p = *0.5-2.5*
Ash particle canting angle mean and deviation m_ϕ (°) and σ_ϕ (°) *TO: Tumbling Orientation, OO: Oblate Orientation* *PO : Prolate Orientation*	*TO: Gaussian PDF* m_ϕ=45°; σ_ϕ=30° *OO: Gaussian PDF* m_ϕ=0°; σ_ϕ=10° *PO: Gaussian PDF* m_ϕ= 90°; σ_ϕ=10°	*TO: Gaussian PDF* m_ϕ=45°; σ_ϕ=30° *OO: Gaussian PDF* m_ϕ=0°; σ_ϕ=10° *PO: Gaussian PDF* m_ϕ=90°; σ_ϕ=10°	*TO: Gaussian PDF* m_ϕ=45°; σ_ϕ=30° *OO: Gaussian PDF* m_ϕ=0°; σ_ϕ=10° *PO: Gaussian PDF* m_ϕ=90°; σ_ϕ=10°	*TO: Gaussian PDF* m_ϕ=45°; σ_ϕ=30° *OO: Gaussian PDF* m_ϕ=0°; σ_ϕ=10° *PO: Gaussian PDF* m_ϕ=90°; σ_ϕ=10°
Non-spherical particle axial ratio r_{ax} (adimensional) RB: basaltic axis ratio RR: rhyolitic axis ratio	r_{ax}=*AR* *RB:* $r_{ax\text{-}b}$ *RR:* $r_{ax\text{-}r}$	r_{ax}=*AR* *RB:* $r_{ax\text{-}b}$ *RR:* $r_{ax\text{-}r}$	r_{ax}=*AR* *RB:* r_{ax}=*1.4* *RR:* r_{ax}=*2.4*	r_{ax}=*AR* *RB:* r_{ax}=*1.4* *RR:* r_{ax}=*2.4*
Dielectric constant $\mathbf{SiO_2}$ weight W_{SiO2} (wt%)	*U-PDF* W_{SiO2}=*50-75%*	*U-PDF* W_{SiO2}=*50-75%*	*U-PDF* W_{SiO2}=*50-75%*	*U-PDF* W_{SiO2}=*50-75%*
Dielectric constant inclusion factor f_i (adimensional)	*Vesicular & non-ves.* *Uniform PDF* f_i=*0-0.3*; $\varepsilon_{ri}=\varepsilon_{rair}$ $\varepsilon_{ra}(f_i,W_{SiO2},\varepsilon_{ri})$	*Vesicular & non-ves.* *Uniform PDF* f_i=*0-0.3*; $\varepsilon_{ri}=\varepsilon_{rair}$ $\varepsilon_{ra}(f_i,W_{SiO2},\varepsilon_{ri})$	*Vesicular & non-ves.* *Uniform PDF* f_i=*0-0.3*; $\varepsilon_{ri}=\varepsilon_{rair}$ $\varepsilon_{ra}(f_i,W_{SiO2},\varepsilon_{ri})$	*Vesicular & non-ves.* *Uniform PDF* f_i=*0-0.3*; $\varepsilon_{ri}=\varepsilon_{rair}$ $\varepsilon_{ra}(f_i,W_{SiO2},\varepsilon_{ri})$

angle m_ϕ; 6) POD canting angle standard deviation σ_ϕ; 7) axial ratio r_{ax}; 8) dielectric constant SiO$_2$ weight W_{SiO2}; and 9) dielectric-constant air-inclusion mass fraction f_i. Table II describes the value range of each parameter as well, either derived from literature [34], [42], [50], [51] or heuristically determined [15].

Following this approach, we can first define a number of ash classes with respect to their average size. The following ash-diameter classes are identified: 1) FA with mean equivalent diameters around 10 μm; 2) CA with mean equivalent diameters around 0.1 mm; 3) SL with mean equivalent diameters around 1 mm; and 4) large lapilli (LL) with mean equivalent diameters around 10 mm. With respect to previous studies [15], we have added the class of LL to take into account agglutinated ash and accidental ballistics.

Each diameter class may be subdivided with respect to other main parameters, e.g., the ash concentration and orientation angle. The model of ash particle properties is complete by considering the following sets of ash subclasses, characterized in Table II.

1) three classes for three different concentrations (C) (small = SC, moderate = MC, and intense = IC);
2) three classes for three different orientations (O) (tumbling = TO, oblate = OO, and prolate = PO);
3) two classes for two different axis ratio models (RB: ratio basaltic–andesitic and RR: ratio rhyolitic)

This means that we can simulate the radar response for each ash size class and for any sets of ash subclasses. Considering each combination, illustrated in Table II, we can obtain 18 different combinations of subclasses for each diameter class (i.e., 18 subclasses for each FA, CA, SL, and LL). In total, we can produce 72 subclasses of backscattering response, consisting of 750 realizations each (for a total of 54 000 simulations), in order to perform our numerical sensitivity analysis with respect to polarimetric signature.

III. ASH PARTICLE BACKSCATTERING AT X-BAND

The scattering Rayleigh regime is not always satisfied since it depends on the ratio between the particle diameter and the radar wavelength λ and the index of refraction of the particle itself [37]. In the general case, the Mie regime has to be taken into consideration. If the Rayleigh assumption is not valid, we can resort to more general solutions of the scattering problem. Later on, we will briefly illustrate the polarimetric radar observables and the simulation results obtained using the T-matrix numerical method, implemented through the Ash Particle Ensemble Scattering Simulator (APESS), which can be

used in the general case of polydispersed randomly oriented spheroidal (ellipsoidal) ash particles [26].

A. Polarimetric Observables

The radar reflectivity factors $Z_{\rm hh}$, $Z_{\rm vv}$, and $Z_{\rm vh}$ at horizontal (h) and vertical (v) polarization states can be expressed in terms of the ash PSD, where the double subscript stands for the received (first index) and transmitted (second index) polarization. If D_e is spherical volume-equivalent diameter and λ is the wavelength, we can define the power radar observables as follows (e.g., [26]–[37]):

$$Z_{xy}=\frac{\lambda^4}{\pi^5|K_p|^2}\int_0^{\pi}\int_0^{\infty}4\pi\left|S_{xy}^{(b)}(D_e,\phi)\right|^2 N_p(D_e)p_p(\phi)$$

$$dD_e\sin\phi d\phi=\frac{\lambda^4}{\pi^5|K_p|^2}\left\langle 4\pi S_{xy}^{(b)}(D_e,\phi)\right\rangle \tag{10}$$

where $S_{xy}^{(b)}$ denotes the backscattering components at x ($x=h,v$ for the receiving mode) and y ($y=h,v$ for the transmitting mode) polarizations of the complex scattering matrix $\mathbf{S}$, K_p is the ash particle radar dielectric factor, and the angle brackets stands for average over the PSD N_p and the POD p_p, assuming a uniform azimuthally symmetric particle orientation. Note the following: 1) $Z_{\rm hv}=Z_{\rm vh}$ for reciprocity and the previous quantities are usually defined in decibels, and 2) the canting angle ϕ is, in general, defined in the plane of polarization of the incident wave with respect to its vertical polarization unit vector. It is equal to the body zenith angle θ_b only for a horizontal incidence, typical of a low elevation angle of ground-based radars.

The derived observables $Z_{\rm dr}$, which is the ratio of reflectivity at the two polarization states, the LDR, and the copolar correlation coefficients $\rho_{\rm hv}$ are defined as (e.g., [26])

$$Z_{\rm dr}=\frac{Z_{\rm hh}}{Z_{\rm vv}}\quad L_{\rm dr}=\frac{Z_{\rm hv}}{Z_{\rm hh}} \tag{11}$$

$$\rho_{\rm hv}=\frac{\left\langle S_{\rm hh}^{(b)}(D_e,\phi)S_{\rm vv}^{(b)*}(D_e,\phi)\right\rangle}{\sqrt{\left\langle\left|S_{\rm hh}^{(b)}(D_e,\phi)\right|^2\right\rangle\left\langle\left|S_{\rm vv}^{(b)}(D_e,\phi)\right|^2\right\rangle}}$$

$$=|\rho_{\rm hv}|e^{j\delta_{\rm hv}} \tag{12}$$

where $\delta_{\rm hv}$ (in degrees) is the volume backscattering differential phase. Note that $Z_{\rm dr}$ and $L_{\rm dr}$ are unitless and usually expressed in decibels (dB).

Another important observable is the specific differential phase shift $K_{\rm dp}$ (in degrees per kilometer) which is due to the forward propagation phase difference between the two polarization and can be obtained from the scattering matrix $\mathbf{S}$ by (e.g., [26])

$$K_{\rm dp}=4\pi\lambda\,{\rm Re}\left[\left\langle S_{\rm hh}^{(f)}(D_e,\phi)\right\rangle-\left\langle S_{\rm vv}^{(f)}(D_e,\phi)\right\rangle\right] \tag{13}$$

where $S_{\rm hh,vv}^{(f)}$ denotes the forward-scattering copolar components of $\mathbf{S}$. Indeed, the radar measures the integral of $K_{\rm dp}$ over a two-way path, namely, the differential phase shift $\Phi_{\rm dp}$ defined as

$$\Phi_{\rm dp}(r)=2\int_0^r K_{\rm dp}(r')\,dr'+\delta_{\rm hv} \tag{14}$$

where r (in kilometers) is the radial path, and it is worthy to note the effect of the phase shift $\delta_{\rm hv}$, due to wave–particle interaction.

The specific power attenuation $\alpha_{\rm hh}$ $(\alpha_{\rm vv})$ at polarization $h(v)$ is, finally, the counterpart of $K_{\rm dp}$ in terms of power attenuation per unit length and can be obtained from (e.g., [26])

$$\alpha_{xy}=2\lambda\,{\rm Im}\left[\left\langle 4\pi S_{xy}^{(f)}(D_e,\phi)\right\rangle\right] \tag{15}$$

$$\alpha_{\rm dp}=8\pi\lambda\,{\rm Im}\left[\left\langle S_{\rm hh}^{(f)}(D_e,\phi)\right\rangle-\left\langle S_{\rm vv}^{(f)}(D_e,\phi)\right\rangle\right] \tag{16}$$

where $\alpha_{\rm dp}$ is the differential propagation specific attenuation. Note that the aforementioned quantities are usually defined in decibels

$$\alpha_{\rm hhdB}(r)=10(Log_{10}e)\,[\alpha_{\rm hh}(r)]=4.343\alpha_{\rm hh}(r) \tag{17}$$

Indeed, the radar measures the integral of $\alpha_{\rm hh}$ $(\alpha_{\rm vv})$ over a one-way path attenuation, namely, the one-way path integrated attenuation $A_{\rm hh}$ $(A_{\rm vv})$, or atmospheric optical thickness, which is defined as

$$A_{xy}(r)=\int_0^r\alpha_{xy}(r')\,dr',\quad A_{\rm dp}(r)=\int_0^r\alpha_{\rm dp}(r')\,dr' \tag{18}$$

where r is the radial path. Note that the aforementioned quantities are usually transformed in decibels, i.e., $A_{\rm hhdB}(r)=4.343\cdot A_{\rm hh}(r)$.

Using APESS for ash radar response, we have assumed spheroidal particles, i.e., ellipsoids with a symmetry axis so that the axial ratio $r_{\rm ax}$, defined in (1), is sufficient to model the shape of the particle itself. If the axis ratio $r_{\rm ax}$ shows an intrinsic variability with a given PDF and variance due to particle oscillations and/or variable AR within the radar volume, it can be shown that the particle nonsphericity can affect the differential reflectivity $Z_{\rm dr}$. The latter is not dependent on the particle concentration and governed by the inverse of reflectivity-weighted axial ratio within the Rayleigh scattering [26]. We can also introduce the effects of the canting angle variability expressed by a G-PDF $p_p(\phi)$ with a zero mean and a standard deviation. The $L_{\rm dr}$ signature will then increase as the canting angle and axial ratio variability will increase. It is worth noting that the differential phase $K_{\rm dp}$ is proportional to the particle concentration C_p, and in case of a particle mixture, $K_{\rm dp}$ will be dominated by the component which will show less tumbling modes, i.e., smaller σ_ϕ. In a way similar to $L_{\rm dr}$, $\rho_{\rm hv}$ is sensitive not only to the diameter-weighted average axial ratio

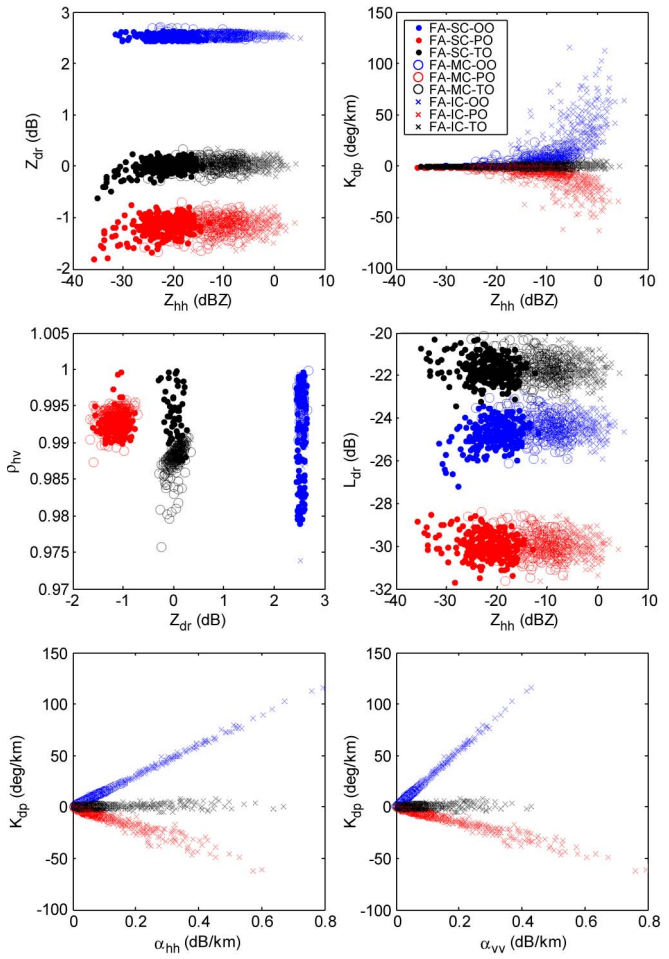

Fig. 4. Correlation between polarimetric radar observables ($Z_{\rm hh}$, $Z_{\rm dr}$, $K_{\rm dp}$, $\rho_{\rm hv}$, $L_{\rm dr}$, $\alpha_{\rm hh}$, and $\alpha_{\rm vv}$; see text for their definitions) for FA size class, different volumetric concentrations (SC, MC, and IC) and different particle orientations (PO, TO, and OO) under the assumption of basaltic–andesitic (RB) particle AR.

but also to their variance. The larger the variance and the mean, the lesser $\rho_{\rm hv}$ will be.

B. Polarimetric Signatures of Particle Size Classes

This section is devoted to the illustration of the ash subclass signatures in terms of polarimetric observables simulated with the aim of understanding which measurement variability may be expected at X-band. We limit our analysis to the latter frequency for the motivation argued within Section I, but, of course, the forward model may be easily adapted to other frequency bands up to the W-band. The correlograms among the radar polarimetric observables are sometimes called "self-consistency" plots [26]–[29]. Indeed, this analysis is aimed at the following: 1) identifying the ash classes which can be actually discriminated with the available measurements and 2) evaluating the cross-correlation and the possible cross-domain of definition among the radar observables in order to perform a powerful quality check of the measurements once acquired and processed by the radar system. We will order this analysis in the following by size classes under the assumption of basaltic axis ratio (RB). Differences due to the assumption of rhyolitic axis ratio (RR) in (1) will be discussed in Section III-D.

The first analysis refers to the FA class in Fig. 4 which corroborates some the following considerations.

1) The copolar reflectivity $Z_{\rm hh}$ supports the discrimination between SC, MC, and IC, but does not alone discriminate concentrations. The differential reflectivity $Z_{\rm dr}$ and LDR $L_{\rm dr}$ clearly distinguish among OO, PO, and TO.
2) The signature of the correlation coefficient $\rho_{\rm hv}$ is not clearly discriminating among the FA subclasses. The differential phase shift $K_{\rm dp}$ is sensitive to both MC and IC and to both OO and PO, particularly for IC. The copolar specific attenuation $\alpha_{\rm hh}$ is linearly correlated with the differential phase shift $K_{\rm dp}$ for OO and PO.

The second analysis refers to the CA class in Fig. 5 which suggests the following comments.

1) The copolar reflectivity $Z_{\rm hh}$ discriminates fairly well between SC, MC, and IC. The differential reflectivity $Z_{\rm dr}$ clearly distinguishes among OO, PO, and TO. The LDR $L_{\rm dr}$ helps to distinguish among OO, PO, and TO, but for MC and IC classes, the confusion increases, particularly for OO.
2) The signature of the correlation coefficient $\rho_{\rm hv}$ may help to discriminate among the PO, OO, and TO subclasses. The differential phase shift $K_{\rm dp}$ is sensitive to both MC and IC and to both OO and PO, particularly for IC. The copolar specific attenuation $\alpha_{\rm hh}$ is nonlinearly correlated with the differential phase shift $K_{\rm dp}$ for OO and PO.

The third analysis refers to the SL class in Fig. 6, providing comments similar to those for the CA class.

1) The copolar reflectivity $Z_{\rm hh}$ is useful to distinguish among SC, MC, and IC. The differential reflectivity $Z_{\rm dr}$ clearly distinguishes among OO, PO, and TO. The LDR $L_{\rm dr}$ is useful to distinguish among OO, PO, and TO.
2) The signature of the correlation coefficient $\rho_{\rm hv}$ may help to discriminate among the PO and OO (the latter overlaps with TO) subclasses when compared with $Z_{\rm dr}$. The differential phase shift $K_{\rm dp}$ is sensitive to both MC and IC and to both OO and PO, particularly for IC. The copolar specific attenuation $\alpha_{\rm hh}$ is nonlinearly correlated with the differential phase shift $K_{\rm dp}$ for OO and PO with a dispersion larger for smaller particle sizes (FA and CA).

The fourth analysis refers to the LL class in Fig. 7. Some further considerations, to be compared with those of the other ash classes, are summarized in the following.

1) The copolar reflectivity $Z_{\rm hh}$ can discriminate among SC, MC, and IC, even though in synergy with other observables. The differential reflectivity $Z_{\rm dr}$ helps to distinguish among OO, PO, and TO, but in a way more confused than those for other size classes. The TO class is fairly confused with the PO class. $L_{\rm dr}$ is more efficient than $Z_{\rm dr}$ to distinguish among orientations, particularly TO.
2) The signature of the correlation coefficient $\rho_{\rm hv}$ does not help to discriminate among the PO, OO, and TO subclasses. $K_{\rm dp}$ is sensitive to both MC and IC, even more for PO than OO, but a very wide dispersion is observed

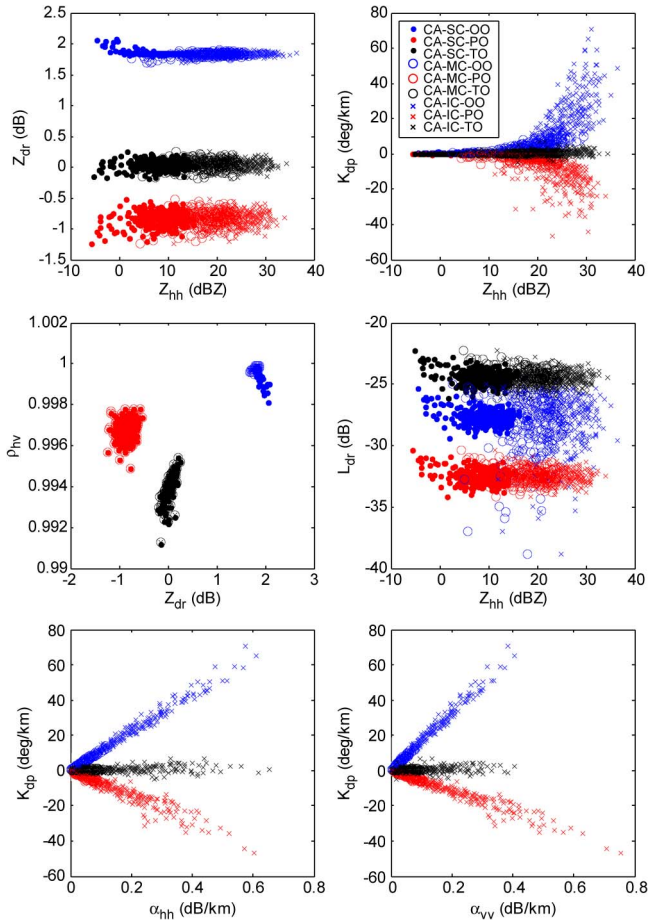

Fig. 5. Same as in Fig. 4, but for CA size class.

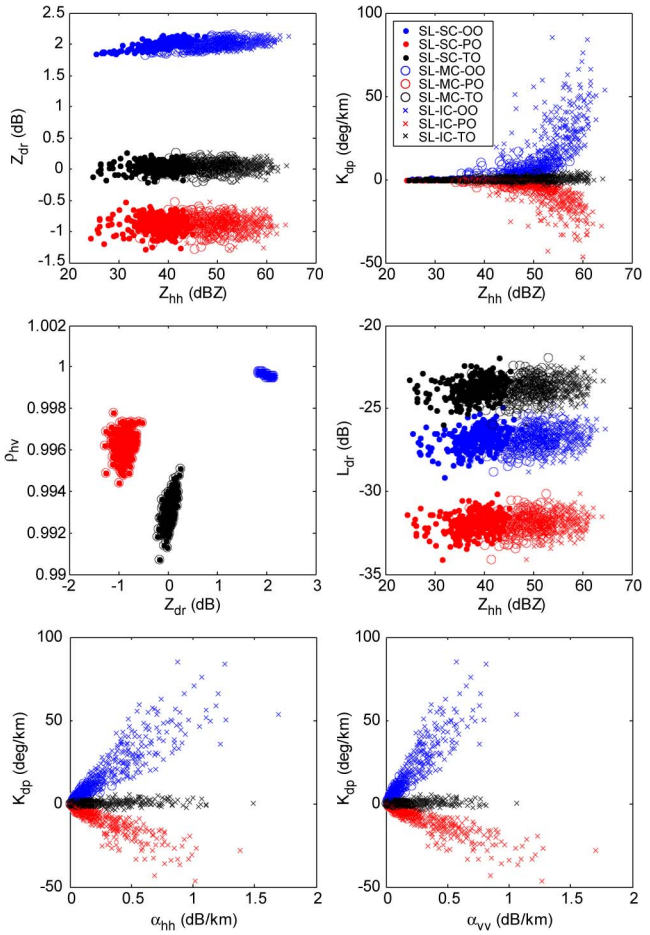

Fig. 6. Same as in Fig. 4, but for SL size class.

compared with smaller particle sizes. The copolar specific attenuation $\alpha_{\rm hh}$ is nonlinearly correlated with the differential phase shift $K_{\rm dp}$, even though the Mie effects tend to reduce this correlation inducing even negative values of $K_{\rm dp}$ for OO and the opposite for PO.

C. Statistical Variability of Polarimetric Signatures

Figs. 4–7 can also highlight the expected statistical variability of the polarimetric radar observables due to ash polydispersions. In this respect, it is worthy to note the following.

1) FA (see Fig. 4) can cause values of $Z_{\rm hh}$ as low as -35 dBZ for very low ash concentrations and up to a few dBZ for intense concentration, whereas values of $Z_{\rm dr}$ may be between -0.5 and 0.5 dB for tumbling FA, while less than -0.5 dB (down to -2 dB) for prolate particles and larger than 0.5 (up to 2.7) for oblate particles, as expected.

   For tumbling FA, $K_{\rm dp}$ is limited within -5°/km and $+5^\circ$/km with a low specific attenuation $\alpha_{\rm hh}$ (less than 0.5 dB/km), a correlation $\rho_{\rm hv}$ between 0.975 and 1.0, and a mean $L_{\rm dr}$ of about -22 dB, whereas for prolate FA, $K_{\rm dp}$ is within 0°/km and -50°/km, associated to a low specific attenuation $\alpha_{\rm hh}$ (less than 0.7 dB/km), a correlation $\rho_{\rm hv}$ between 0.985 and 1.0, and a mean $L_{\rm dr}$ of about -30 dB. For oblate FA, $K_{\rm dp}$ is within 0°/km and 90°/km with a low specific attenuation $\alpha_{\rm hh}$ (less than 0.7 dB/km), a correlation $\rho_{\rm hh}$ larger than 0.975, and a mean $L_{\rm dr}$ of about -22 dB.

2) CA (see Fig. 5) exhibits values of $Z_{\rm hh}$ between -5 and 35 dBZ, going from very low ash concentrations to intense concentration, whereas values of $Z_{\rm dr}$ may be between -0.2 and 0.3 dB for tumbling FA, while less than -0.5 dB (down to -1.3 dB) for prolate particles and larger than 1.5 (up to 2.1) for oblate particles.

   For tumbling FA, $K_{\rm dp}$ is limited within -5°/km and $+5^\circ$/km with a low specific attenuation $\alpha_{\rm hh}$ (less than 0.65 dB/km), a correlation $\rho_{\rm hv}$ between 0.992 and 0.996, and a mean $L_{\rm dr}$ of about -24 dB, whereas for prolate FA, $K_{\rm dp}$ is within 0°/km and -40°/km, associated to a low specific attenuation $\alpha_{\rm hh}$ (less than 0.5 dB/km), a high correlation $\rho_{\rm hh}$ (larger than 0.996), and a mean L_{dr} of about -32 dB. For oblate FA K_{dp} is within 0 and 60°/km with a low specific attenuation $\alpha_{\rm hh}$ (less than 0.5 dB/km), a high correlation $\rho_{\rm hh}$ (larger than 0.998), and a mean $L_{\rm dr}$ of about -23 dB.

3) SL (see Fig. 6) are associated to values of $Z_{\rm hh}$ between as 25 and 63 dBZ, going from very low ash concentrations to intense concentrations, whereas values of $Z_{\rm dr}$ may be between -0.2 and 0.3 dB for tumbling FA, while less than -0.5 dB (down to -1.4 dB) for prolate particles and larger than 1.8 (up to 2.2) for oblate particles.

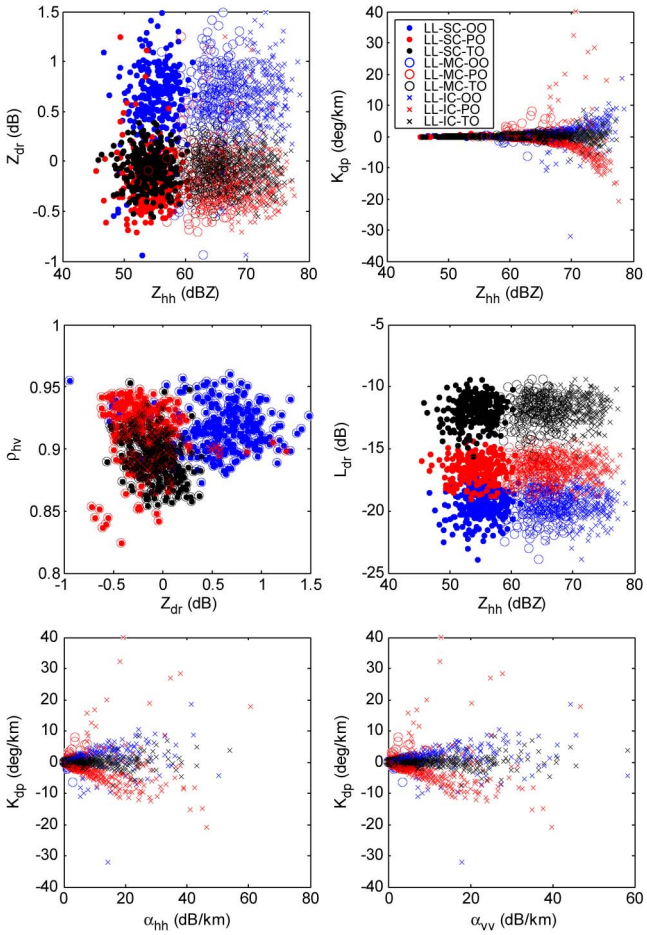

Fig. 7. Same as in Fig. 4, but for LL size class.

For tumbling FA, $K_{\rm dp}$ is limited within -5°/km and $+5^\circ$/km with a specific attenuation $\alpha_{\rm hh}$ less than 1 dB/km, a correlation $\rho_{\rm hv}$ between 0.99 and 0.994, and a mean $L_{\rm dr}$ of about -24 dB, whereas for prolate FA, $K_{\rm dp}$ is within 0°/km and -45°/km with a specific attenuation $\alpha_{\rm hh}$ less than 1 dB/km, a high correlation $\rho_{\rm hh}$ (larger than 0.994), and a mean $L_{\rm dr}$ of about -33 dB. For oblate FA, $K_{\rm dp}$ is within 0°/km and 80°/km with a specific attenuation $\alpha_{\rm hh}$ less than 1.1 dB/km, a high correlation $\rho_{\rm hv}$ (larger than 0.998), and a mean $L_{\rm dr}$ of about -27 dB.

4) LL (see Fig. 7) show values of $Z_{\rm hh}$ between as 45 and 75 dBZ, going from very low ash concentrations to intense concentrations, whereas values of $Z_{\rm dr}$ may be between -0.5 and 0.5 dB for tumbling FA, while less than 1.5 dB (down to -1 dB) for prolate particles and larger than -0.7 (up to 1.5) for oblate particles. This behavior, different from FA, CA, and SL, may be explained by invoking the Mie effects.

For tumbling FA, $K_{\rm dp}$ is limited within -10°/km and $+5^\circ$/km with a relatively high specific attenuation $\alpha_{\rm hh}$ (even larger than 10 dB/km), a relatively low correlation $\rho_{\rm hv}$ (lower than 0.95), and a mean $L_{\rm dr}$ of about -12 dB, whereas for prolate FA, $K_{\rm dp}$ is within -20°/km and 40°/km with a relatively high specific attenuation $\alpha_{\rm hh}$ (even larger than 20 dB/km), a relatively low correlation $\rho_{\rm hv}$ (less than 0.95 down to 0.83), and a mean $L_{\rm dr}$ of about -17 dB. For oblate FA, $K_{\rm dp}$ is within -20°/km and 30°/km with a relatively high specific attenuation $\alpha_{\rm hh}$ (larger than 10 dB/km), a correlation $\rho_{\rm hv}$ between 0.87 and 0.95, and a mean $L_{\rm dr}$ of about -20 dB.

D. Effect of Thepra Chemical Composition

The effect of the axis ratio model can also be numerically evaluated by assuming the rhyolitic (RR) axis ratio, instead of the basaltic–andesitic (RB) one (as mentioned, we neglected the dacite case for lack of data). The type of tephra is an information that can be probably deduced from other *a priori* data. Basaltic and andesitic ash typically contain a SiO_2 content lower than that of the rhyolitic one (see Section II-A). When adopting $r_{\rm ax}$ in (1) for rhyolite with all its limitations, the obtained numerical results (not shown for brevity) suggest the following considerations.

1) The copolar reflectivity $Z_{\rm hh}$ is almost not affected by axis ratio model both within the self-consistency diagrams and the microphysical correlograms.
2) The differential reflectivity $Z_{\rm dr}$ is significantly affected by the change of the axis ratio model, and for both OO and PO, the effect of RB tends to increase and decrease, respectively, the $Z_{\rm dr}$ value.
3) The LDR $L_{\rm dr}$ is strongly affected by the change of the axis ratio model, and for OO, TO, and PO, the effect of RB is to increase the $L_{\rm dr}$ value. The signature of the correlation coefficient $\rho_{\rm hv}$ reduced with respect to the RR case for the PO and TO cases.
4) The differential phase shift $K_{\rm dp}$ is strongly affected by the change of the axis ratio model, and for both OO and PO, the effect of RB is to increase the $K_{\rm dp}$ values.

The previous framework may be considered as the microphysical–electromagnetic basis for designing a model-supervised ash classification algorithm at X-band as an extension of the VARR single-polarization algorithm at C-band previously developed [15]. The same maximum *a priori* probability theoretical framework can be adopted to basically discriminate among the ash diameter subclasses (i.e., FA, CA, SL, and LL) and orientation subclasses (PO, TO, and OO) by assuming that we know the type of thepra and its axial ratio average law.

E. Physical Correlation of Polarimetric Signatures

The usefulness of a radar-based volcanic monitoring of ash clouds is related to the capability of estimating the ash volumetric concentration, as proposed within VARR [15]. Once the ash subclass from the previous step is known, this estimation can be performed by resorting to either nonlinear regression techniques or neural-network approaches.

This section is devoted to the illustration of ash subclass correlation diagrams between the main microphysical quantities, as ash particle concentration C_p (but also, fall rate R_p and the mean diameter $D_{\rm np}$), defined in the previous section, and the main polarimetric radar observables. Some general comments may apply to the numerical results shown in Figs. 8 and 9

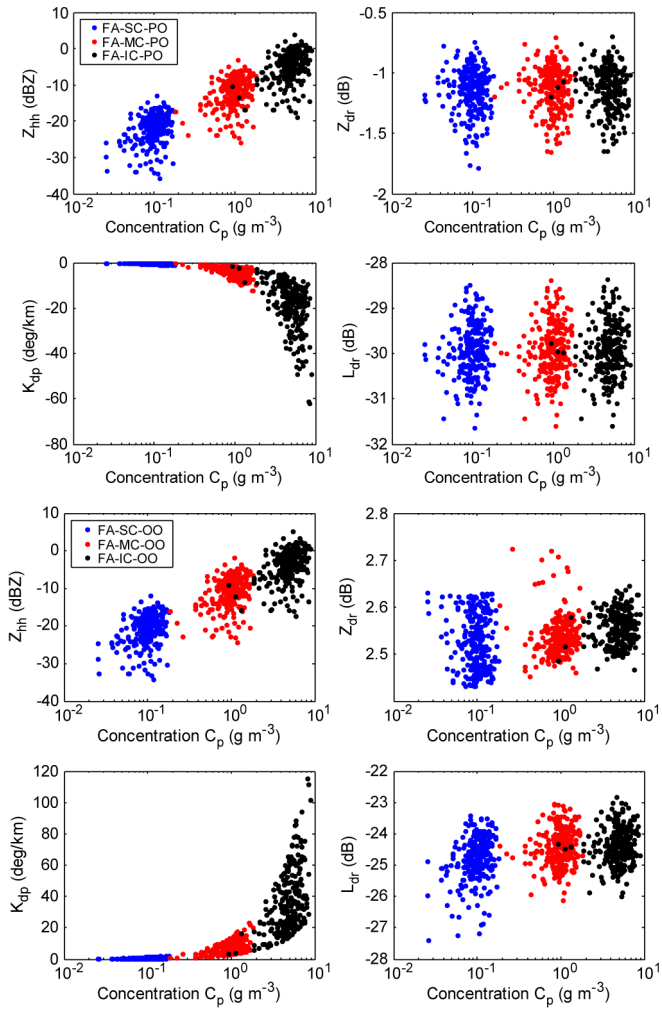

Fig. 8. Correlation between main X-band radar observables ($Z_{\rm hh}$, $Z_{\rm dr}$, $K_{\rm dp}$, and $L_{\rm dr}$; see text for their definitions) and particle ash concentration C_p for (left panels) FA-PO and (right panels) FA-OO classes and SC, MC, and IC under the assumption of RB AR.

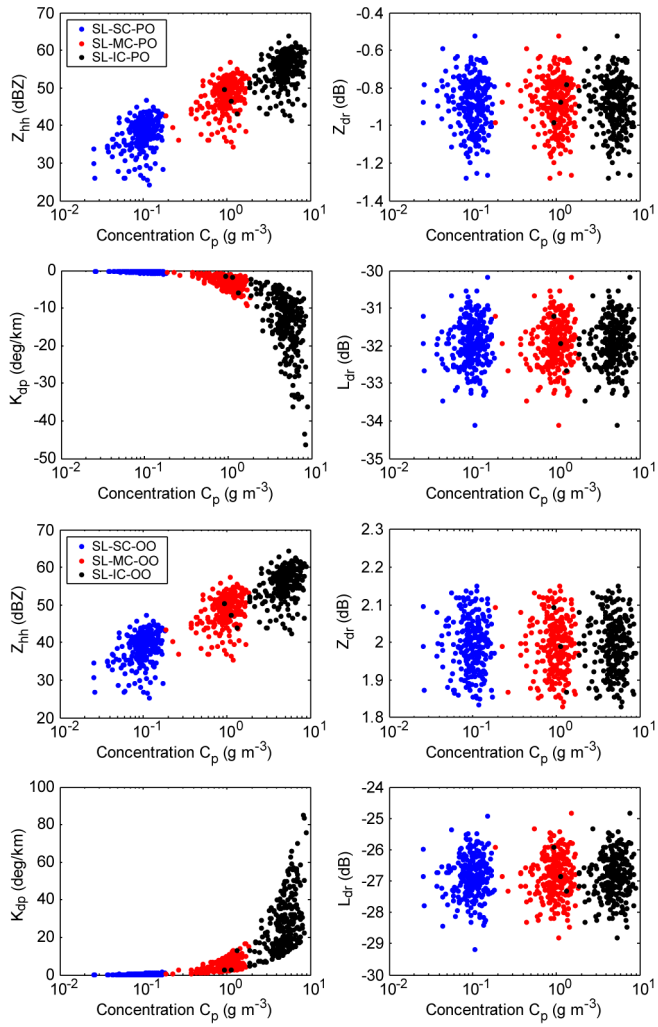

Fig. 9. Same as in Fig. 8, but for SL-PO and SL-OO classes.

for FA and SL classes with PO and OO conditions under the assumption of basaltic axis ratio (RB) as before (for brevity, results for CA and LL classes as well for TO condition are not shown).

1) Ash mass concentration C_p, ashfall rate R_p (not shown for brevity), and mean diameter D_n (not shown for brevity) are almost linearly correlated with copolar reflectivity $Z_{\rm hh}$ for all subclasses. This is, in a way, expected by looking at the Rayleigh relations and even extending to the Mie scattering region for SL and LL.
2) The differential reflectivity $Z_{\rm dr}$ is independent from the concentration and fall rate, as expected, for all subclasses while it is highly sensitive to the particle AR, i.e., its shape. In fact, $Z_{\rm dr}$ strongly varies with TO, PO, and OO orientation models. Moreover, $Z_{\rm dr}$ may depend on $D_{\rm np}$ particularly for PO and OO orientations.
3) The differential phase shift $K_{\rm dp}$ is well negatively and positively correlated with ash concentration C_a and ashfall rate R_a for both PO and OO models, respectively, while a mixed behavior is noticed for TO, the latter being basically a combination of PO and OO.
4) The LDR $L_{\rm dr}$ is not significantly correlated to C_p, $D_{\rm np}$, and R_p, as expected, but is sensitive to the particle orientation.
5) The previous behaviors are almost similar for the considered size classes FA, CA, SL, and LL with some differences on the $D_{\rm np}$ dependence.
6) The dependence on the mean diameter D_n is negatively correlated with $D_{\rm np}$ for FA-OO, positively correlated for CA-OO, and positively correlated for SL-OO and LL-OO.

Analogous comments may be applied to the subclasses of rhyolitic axis ratio RR, considering that the axis ratio trend with the equivalent diameter is opposite to that of the RB case and has much higher values.

From the obtained results, we can conclude that particle concentration, fall rate, and mean diameter can be derived from a combination of $Z_{\rm hh}$ and $K_{\rm dp}$, whereas $Z_{\rm dr}$, $\rho_{\rm hv}$, and $L_{\rm dr}$ may be successfully used to better discriminate the ash classes. Of course, the performances of the X-band polarimetric VARR algorithm (VARR-PX) will be affected by the accuracy and completeness of this polarimetric model of ash radar response. However, on the other hand, any advancement in the understanding of the observed ash clouds can be, in principle,

TABLE III
GENERAL TECHNICAL DATA OF THE X-BAND RADAR SYSTEM

Characteristics	Value			
Antenna beam width	1°			
Antenna gain	44.5 dB			
Operating frequency range	9.36 – 9.38 GHz			
Transmitter peak power	55 kW, single channel			
Min. and Max. Pulse Width	0.3 μs (short)	0.67 μs (medium1)	1.67 μs (medium2)	3.3 μs (long)
MDS	-103 dBm	-106 dBm	-110 dBm	-113 dBm
TX PRF, selectable within range	250 – 2500 Hz	250 – 2500 Hz	250 – 300 Hz	250 – 300 Hz
Range resolution	30 m	100 m	250 m	450 m
Unambiguous range	> 200 km	> 200 km	> 400 km	> 400 km
Range gates per pulse	2500			
Receiver Dynamic/Linearity	90 dB ± 0.5 dB			
Noise figure RX	2.5 dB			
Max. unambiguous velocity	± 80 m/sec (velocity mode)			

incorporated within the VARR-PX in order to improve its validity.

IV. X-BAND SYSTEM SENSITIVITY

A major issue about remote sensing of volcanic ash cloud is the sensitivity to lower values of ash concentration and the optimal choice of its operational mode. These two aspects are, indeed, interconnected as the radar sensitivity is related the inverse square distance, apart from the receiver noise level, space–time sampling, antenna gain, radiowave frequency, and target nature. In this respect, as already proposed in previous works (e.g., Marzano *et al.*, 2006b), we can simulate a schematic volcanic plume and analyze, in a quantitative way, the radar response. In principle, we could construct an ensemble of range profiles of ash clouds supposing to have ash particles with different particle concentration C_p (e.g., SC, MC, and IC), but also with a variable particle mean diameter $D_{\rm np}$ (e.g., FA, CA, SL, or LL) and orientation (e.g., PO, OO, or TO). The problem is that the physical spatial cross-correlation between these parameters is unknown so that the ash plume range profile would be fairly arbitrary. Thus, a conservative solution is to suppose a uniform ash class along the range and vary it for all the identified classes. Of course, we are assuming that all range bins are in visibility and both antenna-beam blocking and ground clutter are avoided through a proper radar data preprocessing.

A. Simulation Environment

The minimum detectable reflectivity (MDZ) for a specified scattering volume at a given range r can be evaluated by assuming a received power equal to the minimum detectable signal MDS_h at horizontal polarization (e.g., [15] and [37])

$$\mathrm{MDZ}_h(r) = C_Z \frac{\lambda^2}{L_{\rm sys}\tau\theta_3\phi_3 G_0^2} \frac{r^2}{P_{\rm th}|K_p|^2} \cdot \mathrm{MDS}_h \qquad (19)$$

where C_Z is a constant, λ is the wavelength, $L_{\rm sys}$ is the system loss, τ is the pulse duration, θ_3 and φ_3 are the antenna zenithal and azimuthal beamwidths, G_0 is the maximum antenna gain, $P_{\rm th}$ is the transmitted peak power, and K_p is the particle dielectric factor. The previous equation takes into account the noise figure of the radar receiver through MDS_h which is generally an available characteristic of a microwave radar system. In an ideal radar, MDS_h will be equal to MDS_v and both will be equal to a given value usually between -100 and -115 dBm (depending on several system factors). Note that MDS_h is, indeed, the sum of the copolar term $\mathrm{MDS}_{\rm hh}$ and the cross-polar term $\mathrm{MDS}_{\rm hv}$, due to vertically polarized transmitted power converted in horizontally polarized received power due to cross-polarization interaction mechanisms. The minimum detectable power analysis can be, of course, converted into a signal-to-noise ratio (SNR) analysis which, for the H-polarized receiving channel, is given by in terms of MDS

$$\begin{aligned}\mathrm{SNR}_h(r) &= \frac{P_{\rm rh}}{\mathrm{MDS}_h} \\ &= P_{\rm th}|K_p|^2 C_Z \frac{\tau\theta_{3h}\phi_{3h}G_{0h}^2}{\lambda^2}\frac{Z_{\rm hh}(r)}{r^2} \\ &\quad \times \frac{L_h^2(r)L_{\rm sysh}}{\mathrm{MDS}_h} \end{aligned} \qquad (20)$$

where $P_{\rm rh}$ is the average received power at H-polarization and L_h is the one-way path attenuation. The general technical data of the X-band radar hardware components we have considered in this work are listed in Table III. The table shows parameters for the short pulse (SP), medium pulse-1 (MP1), medium pulse-2 (MP2), and long pulse (LP) widths corresponding to 0.3-, 0.67-, 1.67-, and 3.3-μs durations, respectively. The system is supposed to be operated within a typical effective range of about 100 km for quantitative retrieval analyses.

From a given ash class and subclass defined in the previous section, a profile of $Z_{\rm hhm}(r)$ and $Z_{\rm vvm}(r)$ can be compared with the corresponding $\mathrm{MDZ}_h(r)$ and $\mathrm{MDZ}_v(r)$, respectively, as a function of the range. On the other hand, the same analysis can be performed using $\mathrm{SNR}_v(r)$ and $\mathrm{SNR}_v(r)$ using $\mathrm{SNR} = 1$ (or 0 dB) as a minimum sensitivity threshold. Just like the microstructure of ash clouds and precipitation, the radar response may vary in space and time, due to various sources of uncertainty: systematic bias in the radar-measured reflectivity due to miscalibration; attenuation from atmospheric gases, ash particles, and rain; incomplete beam filling; ground clutter; vertical air motion, which can induce $C_p - Z$ errors by changing the vertical ash flux and changing the PSD in

TABLE IV
REGRESSION COEFFICIENTS FOR $Z_{\rm hh} - C_p$ STATISTICAL RELATIONS AT X-BAND WHERE $Z_{\rm hh}$ IS IN $\rm mm^6m^{-3}$ AND C_p IS IN $\rm gm^{-3}$

Z_{hh}-C_p relationship						
	TO		OO		PO	
	a_h	b_h	a_h	b_h	a_h	b_h
Fine Ash	0.0707	0.9998	0.0836	1.0001	0.0644	0.9996
Coarse ash	68.817	0.999	80.597	1.011	64.209	0.999
Small Lapilli	67138.98	0.9998	74714.35	1.0003	63359.22	0.9997
Large Lapilli	2682529.35	1.0004	3409298.88	1.0004	2800646.53	1.0016

TABLE V
REGRESSION COEFFICIENTS FOR $Z_{\rm vv} - C_p$ STATISTICAL RELATIONS AT X-BAND WHERE $Z_{\rm hh}$ IS IN $\rm mm^6m^{-3}$ AND C_p IS IN $\rm gm^{-3}$

Z_{vv}-C_p relationship						
	TO		OO		PO	
	a_v	b_v	a_v	b_v	a_v	b_v
Fine Ash	0.0701	0.9978	0.0477	0.9728	0.08373	0.9988
Coarse ash	68.231	1.0001	52.954	1.0124	77.958	1.0001
Small Lapilli	66513.24	1.0001	47188.12	1.0004	77630.99	1.0001
Large Lapilli	2728378.52	1.0001	2948704.67	1.0002	2920470.58	1.0013

vertically inhomogeneous situations; and range and vertical spatial gradients of ash rate.

In order to keep simple the construction of the simplified model for MDZ analysis and considering the scopes of this section, we have considered average $Z_{xx} - C_p$ relations. By using the common radar meteorology approach and using APESS numerical results, we can assume a statistical power-law forward relationship between $Z_{\rm hh}$ or $Z_{\rm vv}$ and C_p, expressed by

$$\begin{cases} Z_{\rm hh} = a_h C_p^{b_h} \\ Z_{\rm vv} = a_v C_p^{b_v} \end{cases} \tag{21}$$

where $a_{h,v}$ and $b_{h,v}$ are the coefficients and $Z_{\rm hh}$ $(Z_{\rm vv})$ is expressed in $\rm mm^6m^{-3}$ and C_p in $\rm gm^{-3}$. The coefficients $a_{h,v}$ and $b_{h,v}$ depend on the frequency, polarization state, and the ash particle microphysical behavior. The same modeling can be easily performed for the specific attenuations $\alpha_{\rm hh}$ and $\alpha_{\rm vv}$.

These regression coefficients in (21) can be determined by performing a least square adjustment between $Z_{\rm hh}$ $(Z_{\rm vv})$ and C_p corresponding value pairs. This coupled data set may be 1) experimentally derived from ground and remote measurements and 2) numerically derived from the APESS simulation environment. Since the experimental sources are really few, if not available at all in a quantitative way so far, we have to resort to APESS simulated data sets. The obtained regression coefficients for (21) are reported in Tables IV and V.

B. System Sensitivity

In our simulation environment, the analysis of SNR range dependence can be easily carried out assuming constant ash concentration along the entire range. In this case, once we have fixed the volcanic ash particle concentration C_p, the ash size class, and their prevailing orientation and polarization along the range and the operational mode, the corresponding polarized equivalent reflectivity factor $Z_{\rm hh}$ and $Z_{\rm vv}$ can be calculated from (21). Then, the received power can be calculated from (20) and compared with the MDS, given in Table III, or, more compactly, expressed in terms of SNR, given in (20), as shown in Figs. 10 and 11. For brevity, the effect of orientation and polarization are evaluated only for tumbling (TO) and horizontal polarization. Similar results are obtained by considering also OO, PO, and vertical polarization as well. Moreover, with SL and LL being always detectable by an X-band weather radar due to their larger mean size, the analysis will be focused only for FA and CA. Path attenuation is always negligible in these cases.

In Fig. 10, the $\rm SNR_h$ for uniform-shaped clouds is shown for CA and constant average concentration values of 0.1, 1, and 5 $\rm g/m^3$. Comparing these plots with the curves in Fig. 11, we can appraise the effect of using LP and SP modes for CA observation. The same analysis is performed for FA ash. As expected, the detection is worse than that for CA under the same conditions. The impact of each operational mode is examined in detail in Fig. 11, where all operational modes are considered for both CA and FA with variable concentration. As expected, the longer is the pulse, the higher is SNR at a given range and concentration.

Taking advantage of the simulation results on the radar sensitivity obtained in the previous and current sections, major recommendations for the utilization of the X-band weather radar up to 100 km are resumed in Table VI and summarized next.

1) SL, LL, and CA can be easily detected. Anyway, for CA and small concentration operational modes, the SP mode should be not used.
2) FA in volcanic cloud scan be detected only for moderate and intense concentrations, and in order to accomplished this detection, the LP or MP2 operational modes should be used. Note that these two modes have a resolution worse than the other two, namely, MP1 and SP.
3) FA and small concentrations cannot be detected beyond 15 km.
4) During routine scans and at the beginning of an eruption crisis, a conservative highly sensitive mode, such as the LP, should be used at first for best detection of dilute cloud of FA.

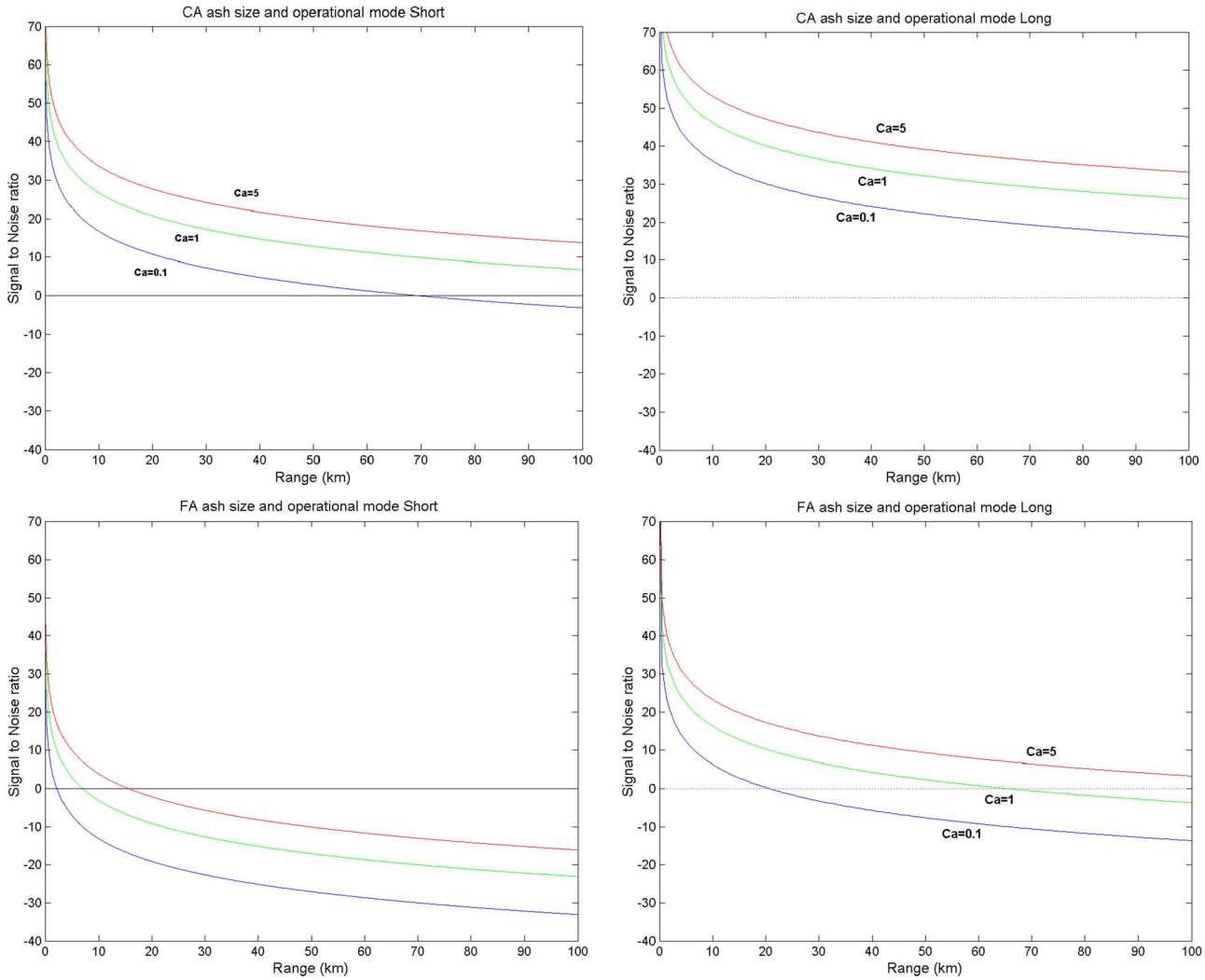

Fig. 10. (Top-left) Effect of concentration on S/N ratio for CA class and operational mode SP as a function of average ash volumetric concentration C_a (0.1, 1, and 5 g/m^3). (Top-right) Same, but for operational mode LP. (Bottom-left) Same, but for FA class and operational mode SP. (Bottom-right) Same for FA class and operational mode LP.

It should be pointed out that, to use LDR data (e.g., as a classifier) with values down to approximately -35 dB, we would need an SNR of at least 35 dB to measure it. Similar situation holds for $\rho_{\rm hv}$, which may be significantly biased for an SNR less than 20 dB.

V. Conclusion

The possibility of monitoring 24 h a day, in all weather conditions, at a fairly high spatial resolution and every few minutes after an eruption is the major advantage of using ground-based microwave radar systems. The latter can be crucial systems to monitor the volcanic eruption from its early stage near the volcano vent, dominated by lapilli and blocks thepra, to its ash-dispersion stage up to a few hundreds of kilometers, dominated by transport and evolution of CA and FA particles. Of course, the sensitivity of the ground-based radar measurements will decrease as the ash cloud will be farther so that, for distances greater than about 50 km, FA might become "invisible" to the radar; but, in this respect, radar observations can be complementary to satellite, lidar, and aircraft observations. Moreover, radar-based products such as real-time erupted volcanic ash concentration, height, mass, and volume can be used to initialize dispersion model inputs.

Due to logistics and space–time variability of the volcanic eruptions, a suggested optimal radar system to detect ash cloud could be a portable X-band weather Doppler polarimetric radar. This radar system can satisfy technological, economical, and the emerging scientific requirements to detect ash cloud. The radar pedestal siting, which is always a problematic tradeoff for a fixed radar system (as the volcano itself may cause a beam obstruction and the plume may advect in unknown directions), can be easily solved by resorting to portable systems.

An overall algorithm for X-band radar polarimetric retrieval of volcanic ash clouds from measured dual-polarization reflectivity can be devised by extending the VARR approach. It can be based on four cascade steps: 1) monitoring of active volcano through a method based on analysis of reflectivity radar data time series associated with *in situ* information and satellite-derived products; 2) tracking of ash plume based on a pattern matching approach applied on radar images; 3) classification of

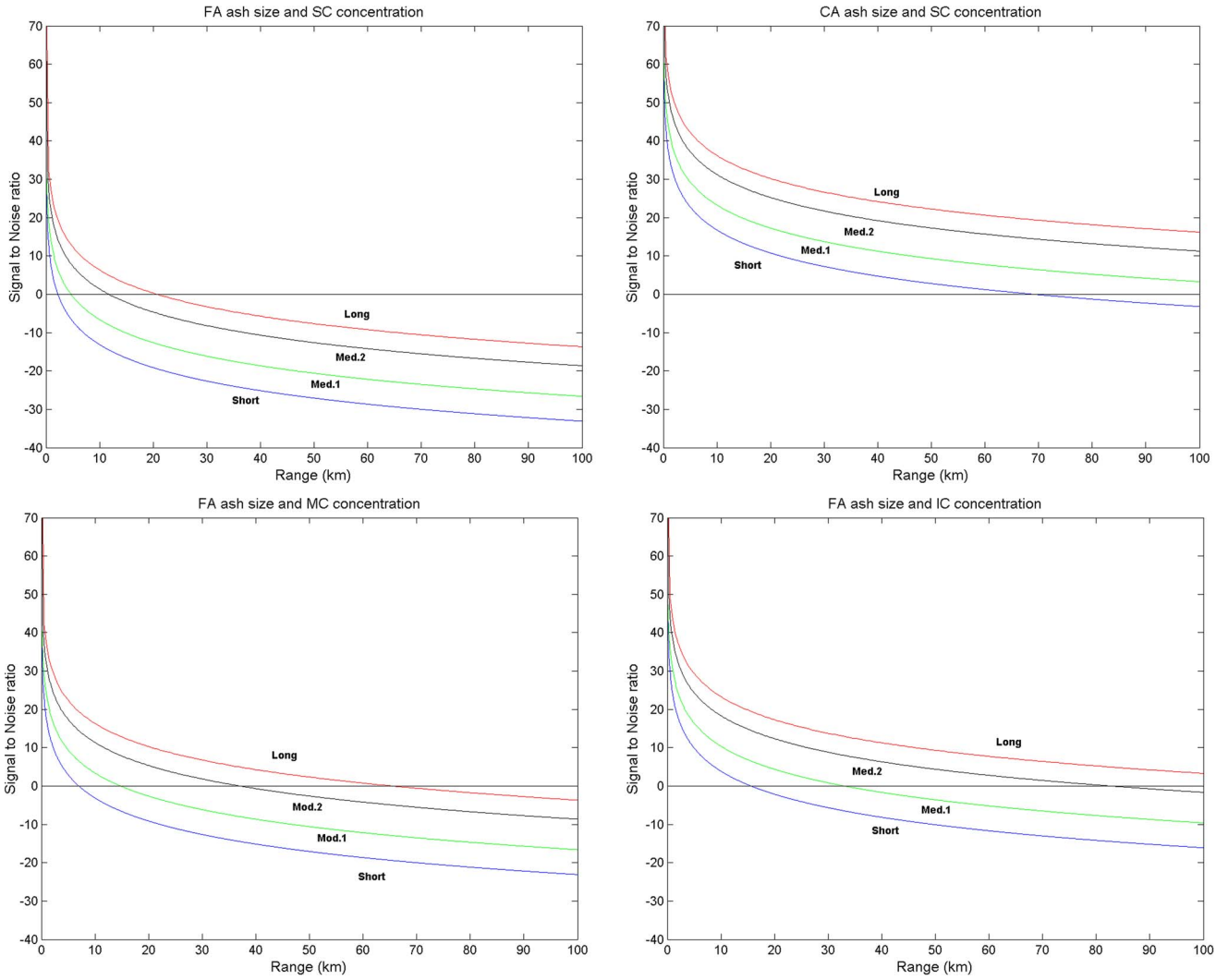

Fig. 11. (Top-left) Effect of the operational mode choice (LP, MP1, MP2, and SP durations; see Table III) on the SNR (in decibels) with FA size class and SC average concentration C_a, equal to 0.1 g/m^3. (Top-right) Same, but for CA and SC classes. (Bottom-left) Same, but for FA and MC average concentration, equal to 1 g/m^3. (Bottom-right) Same, but for FA size class and IC average concentration, equal to 5 g/m^3.

TABLE VI
SUMMARY OF THE SENSITIVITY ANALYSIS RESULTS DERIVED FROM SYNTHETIC UNIFORM-PLUME SCENARIO AND A TYPICAL X-BAND WEATHER RADAR (SEE TABLE II FOR ASH CLASS STATISTICAL VALUES). NOTE THAT LP, MP1, AND MP2 STAND FOR LONG, MEDIUM-1, AND MEDIUM-2 DURATION PULSE MODES, RESPECTIVELY

	Small Concentration (SC)	**Moderate Concentration (MC)**	**Intense Concentration (IC)**
Fine Ash (FA)	Detectable up to 15 km range, using operational LP mode	Detectable up to 45 km, using operational LP mode. using MP2 mode, detection may be up to 20 km.	Detectable up to 85 km using operational LP mode. Using MP2 mode, it can be detected up to 50 km, whereas using MP1 can be detected up to 15 km.
Coarse Ash (CA)	Detectable using any operational mode up to 50 km range. Beyond it can be detected using MP1 and LP operational modes.	Detectable using any operational mode up to 80 km range. Beyond it can be detected using MP1, MP2 and LP operational modes.	Detectable using any operational mode up to 100 km range.
Small Lapilli (SL)	Detectable using any operational mode up to 100 km range.	Detectable using any operational mode up to 100 km range	Detectable using any operational mode up to 100 km range.
Large Lapilli (LL)	Detectable using any operational mode up to 100 km range.	Detectable using any operational mode up to 100 km range.	Detectable using any operational mode up to 100 km range.

ash plume through a method based on the vectorial Bayesian theory; and 4) retrieval of ash amount and fall rate from the measured reflectivity through parametric models. The expected accuracy of the VARR algorithm estimates can be evaluated using a synthetic data set. In order to quantitatively evaluate the ash detectability by weather radars, a sensitivity analysis can be preliminarily performed by simulating a synthetic ash cloud and varying ash concentrations and sizes as functions of the range.

The major recommendation of this paper is that dual-polarization ground-based weather radars can be successfully used for volcanic ash cloud dynamical monitoring and quantitative retrieval of ash category, concentration, and fall rate. Of course, the expected accuracy is conditioned by the microphysical assumptions, chosen to constrain the inverse problem, even though the Bayesian retrieval approach can easily ingest the knowledge of these uncertainties within the VARR scheme. It is intuitive, and it has been demonstrated here that the radar detectability of moderate-to-low concentration FA is improved if, for the same configuration, the available peak power is higher, the radial resolution is larger, and the observation distance is shorter.

Further work is needed to assess the VARR potential using experimental campaign data. Future investigations should be devoted to the analysis of the impact of ash aggregates on microwave radar reflectivity and on the validation of radar estimates of ash amount with ground measurements where available. The last task is not an easy one as the ashfall is dominated by wind advection and by several complicate microphysical processes. This means that what is retrieved by radar within an ash cloud may be not representative of what is collected on the ground in a given area. Spatial integration of ground-collected and radar-retrieved ash amounts should be carried out to make comparisons. Finally, *in situ* collection and recovery of airborne ash from within plumes, possibly with balloons or with newly available robotic aircraft, would improve sample fidelity.

ACKNOWLEDGMENT

The authors would like to thank B. De Bernardinis (formerly at DPCN, Rome, Italy, now at ISPRA, Italy) for his continuous support, R. Hannesen (SelexSI-Gematronik, Germany) for providing the X-band radar technical information, C. M. Riley and W. I. Rose (Michigan Technical University, U.S.) for the access to available volcanic particle measurements, and an anonymous reviewer for the careful reading of the manuscript and useful suggestions.

REFERENCES

[1] R. D. Cadle, A. L. Lazrus, B. J. Huebert, L. E. Heidt, W. I. Rose, D. C. Woods, R. L. Chuan, R. E. Stoiber, D. B. Smith, and R. A. Zielinski, "Atmospheric implications of studies of Central American volcanic eruption clouds," *J. Geophys. Res.*, vol. 84, no. C11, pp. 6961–6968, 1979.

[2] W. I. Rose, D. Delene, D. Schneider, G. Bluth, A. Krueger, I. Sprod, C. McKee, H. Davies, and G. Ernst, "Ice in the 1994 Rabaul eruption cloud: Implications for volcano hazard and atmospheric effects," *Nature*, vol. 375, pp. 477–479, Jun. 1995.

[3] H. F. Graf, M. Herzog, J. M. Oberhuber, and C. Textor, "The effect of environmental conditions on volcanic plume rise," *J. Geophys. Res.*, vol. 104, no. D20, pp. 24 309–24 320, Oct. 1999.

[4] T. J. Casadevall, "Volcanic ash and aviation safety," *U.S. Geol. Surv. Bull.*, no. 2047, pp. 450–469, 1994.

[5] W. I. Rose, "Interaction of aircraft and explosive eruption clouds: A volcanologist's perspective," *AIAA J.*, vol. 25, no. 1, pp. 52–58, 1986.

[6] T. M. Gerlach, M. P. Doukas, K. A. McKee, and R. Kessler, "Airborne detection of diffuse carbon dioxide at Mammoth Montain," *Geophys. Res. Lett.*, vol. 26, pp. 3661–3664, 1999.

[7] W. I. Rose, G. J. S. Bluth, and G. G. J. Ernst, "Integrating retrievals of volcanic cloud characteristics from satellite remote sensors—A summary," *Philos. Trans. Roy. Soc. Lond. A*, vol. 358, no. 1770, pp. 1585–1606, 2000.

[8] D. W. Hillger and J. D. Clark, "Principal component image analysis of MODIS for volcanic ash. Part I: Most important bands and implications for future GOES imagers," *J. Appl. Meteorol.*, vol. 41, no. 10, pp. 985–1001, 2002.

[9] A. J. Prata, "Observations of volcanic ash clouds in the 10–12 micrometer window using AVHRR/2 data," *Int. J. Remote Sens.*, vol. 10, no. 4/5, pp. 751–761, 1989.

[10] S. Wen and W. I. Rose, "Retrieval of sizes and total masses of particles in volcanic clouds using AVHRR bands 4 and 5," *J. Geophys. Res*, vol. 99, no. D3, pp. 5421–5431, 1994.

[11] T. Yu, W. I. Rose, and A. J. Prata, "Atmospheric correction for satellite based volcanic ash mapping and retrievals using 'split-window' IR data from GOES and AVHRR," *J. Geophys. Res*, vol. 107, no. D16, p. 4311, 2002.

[12] R. S. J. Sparks, M. I. Bursik, S. N. Carey, J. S. Gilbert, L. S. Glaze, H. Siggurdsson, and A. W. Woods, *Volcanic Plumes*. New York: Wiley, 1997, p. 574.

[13] D. M. Harris and W. I. Rose, "Estimating particle sizes, concentrations, and total mass of ash in volcanic clouds using weather radar," *J. Geophys. Res.*, vol. 88, no. C15, pp. 10 969–10 983, Dec. 1983.

[14] C. Lacasse, S. Karlsdóttir, G. Larsen, H. Soosalu, W. I. Rose, and G. G. J. Ernst, "Weather radar observations of the Hekla 2000 eruption cloud, Iceland," *Bull. Volcanol.*, vol. 66, no. 5, pp. 457–473, Jul. 2004.

[15] F. S. Marzano, S. Barbieri, G. Vulpiani, and W. I. Rose, "Volcanic ash cloud retrieval by ground-based microwave weather radar," *IEEE Trans. Geosci. Remote Sens.*, vol. 44, no. 11, pp. 3235–3246, Nov. 2006.

[16] M. Hort and R. Seyfried, "Volcanic eruption velocities measured with a micro radar," *Geophys. Res. Lett.*, vol. 25, no. 1, pp. 113–116, 1998.

[17] M. Hort, R. Seyfried, and M. Vöge, "Radar Doppler velocimetry of volcanic eruptions: Theoretical considerations and quantitative documentation of changes in eruptive behaviour at Stromboli volcano, Italy," *Geophys. J. Int.*, vol. 154, no. 2, pp. 515–532, Aug. 2003.

[18] M. Gouhier and F. Donnadieu, "Mass estimations of ejecta from Strombolian explosions by inversion of Doppler radar measurements," *J. Geophys. Res.*, vol. 113, pp. B10 202–B10 219, 2008.

[19] M. Gouhier and F. Donnadieu, "The geometry of Strombolian explosions: Insights from Doppler radar measurements," *Geophys. J. Int.*, vol. 154, pp. 515–532, 2003.

[20] V. Matthias and J. Bösenberg, "Aerosol climatology for the planetary boundary layer derived from regular lidar measurements," *Atmos. Res.*, vol. 63, no. 3/4, pp. 221–245, Aug. 2002.

[21] G. Pappalardo, A. Amodeo, L. Mona, M. Pandolfi, N. Pergola, and V. Cuomo, "Raman lidar 248 observations of aerosol emitted during the 2002 Etna eruption," *Geophys. Res. Lett.*, vol. 31, no. L05 120, p. 249, 2004, doi: 10.1029/2003GL019073.

[22] F. S. Marzano, S. Barbieri, E. Picciotti, and S. Karlsdóttir, "Monitoring sub-glacial volcanic eruption using C-band radar imagery," *IEEE Trans. Geosci. Remote Sens.*, vol. 48, no. 1, pp. 403–414, Jan. 2010.

[23] J. Wood, C. Scott, and D. Schneider, "WSR-88D radar observations of volcanic ash, world meteorological organization," in *Proc. 4th Int. Workshop Ash, VAWS/4 WP/04-03*, Rotorua, New Zealand, Mar. 26–30, 2007, pp. 1–9.

[24] F. S. Marzano, G. Vulpiani, and W. I. Rose, "Microphysical characterization of microwave radar reflectivity due to volcanic ash clouds," *IEEE Trans. Geosci. Remote Sens.*, vol. 44, no. 2, pp. 313–327, Feb. 2006.

[25] T. A. Seliga and V. N. Bringi, "Potential use of radar reflectivity measurements at orthogonal polarizations for measuring precipitation," *J. Appl. Meteor.*, vol. 15, no. 1, pp. 69–76, 1976.

[26] V. N. Bringi and V. Chandrasekar, *Polarimetric Doppler Weather Radar: Principles and Applications*. Cambridge, U.K.: Cambridge Univ. Press, 2001.

[27] J. M. Straka, D. S. Zrnic, and A. V. Ryzhkov, "Bulk hydrometeor classification and quantification using polarimetric radar data: Synthesis of relations," *J. Appl. Meteor.*, vol. 39, no. 8, pp. 1341–1372, Aug. 2000.
[28] E. Gorgucci, V. Chandrasekar, V. N. Bringi, and G. Scarchilli, "Estimation of raindrop size distribution parameters from polarimetric radar measurements," *J. Atmos. Ocean. Technol.*, vol. 59, no. 15, pp. 2373–2384, Aug. 2002.
[29] F. S. Marzano, D. Scaranari, and G. Vulpiani, "Supervised fuzzy-logic classification of hydrometeors using C-band weather radars," *IEEE Trans. Geosci. Remote Sens.*, vol. 45, no. 11, pp. 3784–3799, Nov. 2007.
[30] W. I. Rose, R. L. Chuan, and D. C. Woods, "Small particles in plumes of Mount St. Helens," *J. Geophys. Res.*, vol. 87, no. C7, pp. 4956–4962, Jun. 1982.
[31] D. C. Woods, R. L. Chuan, and W. I. Rose, "Halite particles injected into the stratosphere by the 1982 El Chichón eruption," *Science*, vol. 230, no. 4722, pp. 170–172, Oct. 1985.
[32] R. L. Chuan, J. Palais, W. I. Rose, and P. R. Kyle, "Fluxes, sizes, morphology and compositions of particles in the Mt. Erebus volcanic plume, December 1983," *J. Atmos. Chem.*, vol. 4, no. 4, pp. 467–477, Dec. 1986.
[33] J. Taddeucci and M. Palladino, "Particle size-density relationship in pyroclastic deposit: Inference for emplacement processes," *Bull. Volcanol.*, vol. 64, pp. 273–284, May 2002.
[34] C. M. Riley, W. I. Rose, and G. J. S. Bluth, "Quantitative shape measurements of distal volcanic ash," *J. Geophys. Res.*, vol. 108, no. B10, pp. 2504–2514, 2003.
[35] C. Textor, H.-F. Graf, M. Herzog, J. M. Oberhuber, W. I. Rose, and G. G. J. Ernst, "Volcanic particle aggregation in explosive eruption columns Part I: Parameterization of the microphysics of hydrometeors and ash," *J. Volcanol. Geotherm. Res*, vol. 150, no. 4, pp. 359–377, Feb. 2005.
[36] N. Krotkov, D. Flittner, and A. Krueger, "Effect of particle non-sphericity on satellite monitoring of drifting volcanic ash clouds," *J. Quant. Spectrosc. Radiat. Trans.*, vol. 63, no. 2–6, pp. 613–630, Sep. 1999.
[37] H. Sauvageot, *Radar Meteorology*. Norwell, MA: Artech House, 1992.
[38] S. Y. Matrosov, K. A. Clark, B. E. Martner, and A. Tokay, "X-Band polarimetric radar measurements of rainfall," *J. Appl. Meteor.*, vol. 41, no. 9, pp. 941–952, 2002.
[39] S. G. Park, V. N. Bringi, V. Chandrasekar, M. Maki, and K. Iwanami, "Correction of radar reflectivity and differential reflectivity for rain attenuation at X band—Part I: Theoretical and empirical basis," *J. Atmos. Ocean. Technol.*, vol. 22, no. 11, pp. 1621–1632, Nov. 2005.
[40] M. N. Anagnostou, E. N. Anagnostou, G. Vulpiani, M. Montopoli, F. S. Marzano, and J. Vivekanandan, "Evaluation of X-band polarimetric radar estimates of drop size distributions from coincident S-band polarimetric estimates and measured raindrop spectra," *IEEE Trans. Geosci. Remote Sens.*, vol. 46, no. 10, pp. 3067–3075, Oct. 2008.
[41] G. G. J. Ernst, M. I. Bursik, S. N. Carey, and R. S. J. Sparks, "Sedimentation from turbulent jets and plumes," *J. Geophys. Res.*, vol. 101, no. B3, pp. 5575–5589, 1996.
[42] K. H. Wohletz, M. F. Sheridan, and W. K. Brown, "Particle size distributions and the sequential fragmentation/transport-theory applied to volcanic ash," *J. Geophys. Res.*, vol. 94, no. B11, pp. 15 703–15 721, 1989, doi: 10.1029/JB094iB11p15703.
[43] P. Dellino and L. La Volpe, "Cluster analysis of ash particles morphology features to discriminate fragmentation dynamics in explosive eruptions," *Acta Vulcanologica*, vol. 8, no. 1, pp. 31–39, 1996.
[44] J. R. Riehle, W. I. Rose, D. J. Schneider, T. J. Casadevall, and J. S. Langford, "Unmanned aerial sampling of a volcanic ash cloud," *EOS Trans. Amer. Geophys. Union*, vol. 75, no. 12, pp. 137–138, 1994.
[45] W. I. Rose and A. J. Durant, "Fine ash content of explosive eruptions," *J. Volcanol. Geotherm. Res.*, vol. 186, no. 1/2, pp. 32–39, Sep. 2009.
[46] D. Pieri, C. Ma, J. J. Simpson, G. Hufford, T. Grindle, and C. Grove, "Analyses of in-situ airborne volcanic ash from the February 2000 eruption of Hekla Volcano, Iceland," *Geophys. Res. Lett.*, vol. 29, no. 16, pp. 1767–1770, 2002.
[47] W. I. Rose and C. A. Chesner, "Dispersal of ash in the great Toba eruption, 75,000 years B.C.," *Geology*, vol. 15, pp. 913–917, 1987.
[48] J. Zhao, R. P. Turco, and O. B. Toon, "A model simulation of Pinatubo volcanic aerosols in stratosphere," *J. Geophys. Res.*, vol. 100, no. D4, pp. 7315–7328, 1995.
[49] M. Stracquadanio, E. Dinelli, and C. Trombini, "Role of volcanic dust in the atmospheric transport and deposition of polycyclic aromatic hydrocarbons and mercury," *J. Environ. Monit.*, vol. 5, no. 6, pp. 984–988, Dec. 2003.
[50] M. Coltelli, L. Miraglia, and S. Scollo, "Characterization of shape and terminal velocity of tephra particles erupted during the 2002 eruption of Etna volcano, Italy," *Bull. Volcanol.*, vol. 70, no. 9, pp. 1103–1112, Sep. 2008, doi: 10.1007/s00445-007-0192-8.
[51] R. Adams, W. F. Perger, W. I. Rose, and A. Kostinski, "Measurements of the complex dielectric constant of volcanic ash from 4 to 19 GHz," *J. Geophys. Res.*, vol. 101, no. B4, pp. 8175–8185, 1996.
[52] M. Gouhier and F. Donnadieu, "The geometry of Strombolian explosions: Insights from Doppler radar measurements," *Geophys. J. Int.*, vol. 183, no. 3, pp. 1376–1391, Dec. 2010.

Frank Silvio Marzano (S'89–M'99–SM'03) received the Laurea degree (*cum laude*) in electrical engineering and the Ph.D. degree in applied electromagnetics from Sapienza University of Rome, Rome, Italy, in 1988 and 1993, respectively.

After being with the Italian Space Agency (ASI) and being a Lecturer with the University of Perugia, Perugia, Italy, in 1997, he joined the Department of Electrical Engineering and cofounded CETEMPS, University of L'Aquila, L'Aquila, Italy. In 2005, he joined the Department of Electronic Engineering (currently the Department of Information Engineering, Electronics and Telecommunications), Sapienza University of Rome, where he currently teaches courses on antenna theory, electromagnetic propagation, and remote sensing. Since 2007, he has also been Vice Director of CETEMPS. His current research concerns passive and active remote sensing of the atmosphere from ground-based, airborne, and spaceborne platforms, development of inversion methods, radiative transfer modeling of scattering media, and radar meteorology issues. He is also involved in radio and optical propagation topics in relation to incoherent wave modeling, scintillation prediction, and rain fading analysis along terrestrial and satellite links. He has published 100 papers on international refereed journals, 30 book chapters, and more than 200 extended abstracts in conference proceedings. He coedited two books on remote sensing for *Springer-Verlag*, Berlin, Germany, in 2002 and 2010. He is a Reviewer for major international journals in remote sensing, geoscience, and propagation. Since January 2004, he has been acting as an Associated Editor of the IEEE GEOSCIENCE REMOTE SENSING LETTERS. Since 2011, he has also been the Associate Editor of the European Geosciences Union (EGU) *Atmospheric Measurement Techniques* journal. In 2005 and 2007, he has been Guest Coeditor of the MicroRad04 and MicroRad06 Special Issues for the IEEE TRANSACTIONS ON GEOSCIENCE AND REMOTE SENSING.

Dr. Marzano is an IEEE senior member of the Geoscience and Remote Sensing Society. In 1993, he was the recipient of the Young Scientist Award of the XXIV General Assembly of the Union Radio-Scientifique Internationale (Osaka, Japan). In 1998, he was the recipient of the ARPAD Award from the Naval Research Laboratory (Washington, DC, U.S.), whereas in 2008, he received the Best Paper Award from the EGU Plinius Conference (Nicosia, Cyprus) and, in 2009, the Best Oral Paper Award on propagation from the European Conference on Antennas and Propagation (Berlin, German). Within 2001–2005, he was the Italian national delegate for the European COST actions numbers 720 and 280; since 2008, he has been the national delegate for the European COST Action project ES702 "EGCliMet" and COST Action project IC0802 "PropTNEO." Since 2010, he has been a member of the European Volcanic Ash Cloud Expert Group.

Errico Picciotti received the Laurea degree (*cum laude*) in electrical engineering from the University of Ancona, Ancona, Italy, in 1992.

In 1997, he joined the Science and Technology Park of Abruzzo, L'Aquila, Italy, as a Radar Meteorologist. In 2002, he became a Researcher within CETEMPS, working on radar systems and polarimetry. Since 2007, he has been working with HIMET, L'Aquila, where he became the Coordinator of the radar meteorology division.

Gianfranco Vulpiani (M'06) received the Laurea degree in physics and the Ph.D. degree in radar meteorology from the University of L'Aquila, L'Aquila, Italy, in 2001 and 2005, respectively.

In 2001, he was with the Department of Physics and CETEMPS, University of L'Aquila, where he was a Research Scientist on ground-based radar meteorology, with special focus on C-band applications and polarimetric applications. He was a Visiting Scientist with Colorado State University, Fort Collins, in 2004. In 2006, he was with the Department of Observation Systems, Météo-France, Paris, France, where he was a Postdoctoral Researcher. Within the framework of the European project FLYSAFE, he has worked on the development of dual-polarization retrieval techniques with a special focus on attenuation correction and hail detection. Since March 2007, he has been with the National Department of Civil Protection, Rome, Italy, where he is in charge of managing the Italian radar network. He is a Reviewer for several international journals in remote sensing topics.

Mario Montopoli received the Laurea degree in electronic engineering from the University of L'Aquila, L'Aquila, Italy, in 2004. In 2005, he started the Ph.D. program on radar meteorology within a joint program between the University of Basilicata, Potenza, Italy, and Sapienza University of Rome, Rome, receiving the degree in 2008.

In 2005, he joined CETEMPS as a Research Scientist on ground-based radar meteorology and microwave remote sensing. Since 2006, he has also been a Research Assistant with the Department of Electrical and Information Engineering, University of L'Aquila. His main interests are on precipitation retrieval, C-band radar applications and processing techniques, and spaceborne radiometry for Earth and planetary observations.

Dr. Montopoli was the recipient of the Best Oral Paper Award on propagation from the European Conference on Antennas and Propagation (Berlin, German), in 2009 and the Young Scientist Best Paper Award from the European Conference on Radar in Meteorology and Hydrology (Sibiu, Romania) in 2010.